# CFD–DEM Modeling of Gas Fluidization of Fine Ellipsoidal Particles

**Jieqing Gan, Zongyan Zhou, and Aibing Yu**
Laboratory for Simulation and Modeling of Particulate Systems, Dept. of Chemical Engineering, Monash University, Victoria 3800, Australia

*DOI 10.1002/aic.15050*
*Published online October 1, 2015 in Wiley Online Library (wileyonlinelibrary.com)*

*Particle characteristics are important factors affecting gas fluidization. In this work, the effects of both particle size and shape on fluidization in different flow regimes are studied using the combined computational fluid dynamic–discrete element method approach. The results are first analyzed in terms of flow patterns and fluidization parameters such as pressure drop, minimum fluidization, and bubbling velocities. The results show that with particle size decreasing, agglomerates can be formed for fine ellipsoidal particles. In particular, "chain phenomenon," a special agglomerate phenomenon exists in expanded and fluidized beds for fine prolate particles, which is caused by the van der Waals force. The minimum fluidization velocity increases exponentially with the increase of particle size, and for a given size, it shows a "W" shape with aspect ratio. A correlation is established to describe the dependence of minimum fluidization velocity on particle size and shape. Ellipsoids have much higher minimum bubbling velocities and fluidization index than spheres.* © 2015 American Institute of Chemical Engineers *AIChE J*, 62: 62–77, 2016
*Keywords: discrete element method, fluidization, fine particles, ellipsoids*

## Introduction

Fluidization operations are widely used in many industries, for example, cement, food, and pharmaceutical industries. Fluidization quality is closely related to particle characteristics such as size and shape. Understanding the effects of particle characteristics is of vital importance for better design and control of fluidization operations under different conditions. In the past decades, extensive investigations have been performed in this direction, particularly for the fluidization of fine spherical particles.[1–5] Generally, three flow regimes (fixed, expanded, and fluidized beds) exist for cohesive fine particles, and two regimes (fixed and fluidized beds) for noncohesive coarse particles.[6] Particularly, there is an interval of nonbubbling expansion for fine particles between the minimum fluidization velocity $U_{mf}$ and the minimum bubbling velocity $U_{mb}$. Many experimental[7–9] and numerical[10,11] studies have been conducted focusing on these flow regimes. Fluidization parameters such as pressure drop,[5,10] minimum fluidization,[12–15] and bubbling velocities,[3,7,11,16–18] and bed expansion ratio, are usually used to characterize these flow regimes. Different correlations have been proposed to predict $U_{mf}$ as a function of particle density and size, fluid density and viscosity, as summarized by Suksankraisorn et al.[19] Phase diagrams in terms of particle diameter and velocity are used to determine the transition between flow regimes.[9] Other phase diagrams in terms of coordination number-bed porosity relationships[20] can also be used, which shows two branches representing expanded and fluidized (bed) states. Criterion for the bed expansion has been established in terms of particle and particle–fluid interaction forces.[12,20]

However, so far, most of the studies deal with spherical particles. The resulting findings are useful, but may have limitation in addressing practical problems. In reality, most particles are nonspherical, of either regular or irregular shapes. However, because of the difficulty in representing irregular shapes and heavy computational requirement, relatively few studies are concerned with nonspherical particles, with majority limited to simple regular shapes and not systematic. Particle shape is one of the most important factors that significantly affects the packing properties, fluidization behavior,[21,22] and even heat transfer performance.[23,24] For gas fluidization, significant differences can be observed for the pressure drop varying with particle shapes.[25] Liu et al.[21] showed that nonspherical particles give poor fluidizing quality as compared to spherical particles in terms of pressure drop and $U_{mf}$. Hilton et al.[26] also demonstrated that particle shape has a significant effect on the dynamics of the fluidized bed including increased pressure gradients and lower fluidization velocities when compared to beds of spherical particles. Zhou et al.[22] showed that particle shape affects bed permeability and minimum fluidization velocity significantly. Moreover, segregation[27] and mixing[28] behaviors are also strongly influenced. Various drag coefficients[29–31] are proposed to take into account the effect of particle shape. Notwithstanding, there is still rare concern on fluidization of fine nonspherical powders, which are widely used in industrial fluidized beds, such as fluidized catalytic creaking riser and circulating fluidized bed boiler. Many fundamental questions are not clear for fluidization of cohesive nonspherical particles. For example, are there any difference

Correspondence concerning this article should be addressed to Z.Y. Zhou at Zongyan.Zhou@monash.edu.

**Table 1. Components of Forces and Torque Acting on Particle *i***

| Forces and Torques | Symbols | Equations |
|---|---|---|
| Normal elastic force | $\mathbf{f}_{\mathrm{cn},ij}$ | $-4/3E^*\sqrt{R^*}\boldsymbol{\delta}_{\mathrm{n}}^{3/2}\mathbf{n}$ |
| Normal damping force | $\mathbf{f}_{\mathrm{dn},ij}$ | $-c_{\mathrm{n}}(8m_{ij}E^*\sqrt{R^*\boldsymbol{\delta}_{\mathrm{n}}})^{1/2}\mathbf{v}_{\mathrm{n},ij}$ |
| Tangential elastic force | $\mathbf{f}_{\mathrm{ct},ij}$ | $-\mu_{\mathrm{s}}\lvert\mathbf{f}_{\mathrm{cn},ij}\rvert(1-(1-\boldsymbol{\delta}_{\mathrm{t}}/\boldsymbol{\delta}_{\mathrm{t,max}})^{3/2})\hat{\boldsymbol{\delta}}_{\mathrm{t}}\ (\boldsymbol{\delta}_{\mathrm{t}}<\boldsymbol{\delta}_{\mathrm{t,max}})$ |
| Tangential damping force | $\mathbf{f}_{\mathrm{dt},ij}$ | $-c_{\mathrm{t}}(6\mu_{\mathrm{s}}m_{ij}\lvert\mathbf{f}_{\mathrm{cn},ij}\rvert\sqrt{1-\lvert\boldsymbol{\delta}_{\mathrm{t}}\rvert/\boldsymbol{\delta}_{\mathrm{t,max}}}/\boldsymbol{\delta}_{\mathrm{t,max}})^{1/2}\mathbf{v}_{\mathrm{t},ij}\ (\boldsymbol{\delta}_{\mathrm{t}}<\boldsymbol{\delta}_{\mathrm{t,max}})$ |
| Coulomb friction force | $\mathbf{f}_{\mathrm{t},ij}$ | $-\mu_{\mathrm{s}}\lvert\mathbf{f}_{\mathrm{cn},ij}\rvert\hat{\boldsymbol{\delta}}_{\mathrm{t}}\ (\boldsymbol{\delta}_{\mathrm{t}}\geq\boldsymbol{\delta}_{\mathrm{t,max}})$ |
| Torque by normal force | $\mathbf{M}_{\mathrm{n},ij}$ | $\mathbf{R}_{ij}\times(\mathbf{f}_{\mathrm{cn},ij}+\mathbf{f}_{\mathrm{dn},ij})$ |
| Torque by tangential force | $\mathbf{M}_{\mathrm{t},ij}$ | $\mathbf{R}_{ij}\times(\mathbf{f}_{\mathrm{ct},ij}+\mathbf{f}_{\mathrm{dt},ij})$ |
| Rolling friction torque | $\mathbf{M}_{\mathrm{r},ij}$ | $\mu_{\mathrm{r},ij}\lvert\mathbf{f}_{\mathrm{n},ij}\rvert\hat{\boldsymbol{\omega}}_{\mathrm{t},ij}^{\mathrm{n}}$ |
| Fluid drag force | $\mathbf{f}_{\mathrm{d},i}$ | $0.125C_{\mathrm{d0},i}\rho_{\mathrm{f}}\pi d_{\mathrm{pi}}^2\varepsilon_i^2\lvert\mathrm{u}_i-\mathrm{v}_i\rvert(\mathrm{u}_i-\mathrm{v}_i)\varepsilon_i^{-\chi}$ |

Where, $1/m_{ij}=1/m_i+1/m_j$, $1/\mathrm{R}^*=1/\lvert\mathrm{R}_i\rvert+1/\lvert\mathrm{R}_j\rvert$, $E^*=E/2(1-\nu^2)$, $\hat{\boldsymbol{\omega}}_{\mathrm{t},ij}=\boldsymbol{\omega}_{\mathrm{t},ij}/\lvert\boldsymbol{\omega}_{\mathrm{t},ij}\rvert$, $\hat{\boldsymbol{\delta}}_{\mathrm{t}}=\boldsymbol{\delta}_{\mathrm{t}}/\lvert\boldsymbol{\delta}_{\mathrm{t}}\rvert$, $\boldsymbol{\delta}_{\mathrm{t,max}}=\mu_{\mathrm{s}}(2-\nu)/2(1-\nu)\cdot\boldsymbol{\delta}_{\mathrm{n}}$, $\mathbf{v}_{ij}=\mathbf{v}_j-\mathbf{v}_i+\boldsymbol{\omega}_j\times\mathbf{R}_j-\boldsymbol{\omega}_i\times\mathbf{R}_i$, $\mathbf{v}_{\mathrm{n},ij}=(\mathbf{v}_{ij}\cdot\mathbf{n})\cdot\mathbf{n}$, $\mathbf{v}_{\mathrm{t},ij}=(\mathbf{v}_{\mathrm{t},ij}\times\mathbf{n})\times\mathbf{n}$, $\chi=3.7-0.65\exp[-1-(1.5-\log_{10}\mathrm{Re}_i)^2/2$, and $\mathrm{Re}_i=\rho_{\mathrm{f}}d_{\mathrm{pi}}\varepsilon_i\lvert\mathbf{u}_i-\mathbf{v}_i\rvert/\mu_{\mathrm{f}}$.
Note that tangential forces ($\mathbf{f}_{\mathrm{ct},ij}+\mathbf{f}_{\mathrm{dt},ij}$) should be replaced by $\mathbf{f}_{\mathrm{t},ij}$ when $\boldsymbol{\delta}_{\mathrm{t}}>\boldsymbol{\delta}_{\mathrm{t,max}}$.

in flow regimes between spheres and nonspherical particles? How do particles of different sizes and shapes interact with each other when particle size varies from millimeters to microns? Are the existing correlations for minimum fluidization velocity still suitable for nonspherical particles?

To answer these questions, an ideal approach is to use discrete element modeling, for example, the combined computational fluid dynamics (CFDs) with discrete element method (DEM), as demonstrated in the recent numerous studies of fluidization.[32,33] CFD–DEM has increasingly played significant roles in the study of particle–fluid flow fundamentals. In this approach, the solid phase is based on the DEM, and gas phase is treated as a continuum phase in a similar way to the two fluid model. CFD–DEM has its unique advantage in studying the macro and microfluidization behavior. In particular, it can track the motion of each particle in the system, thus can be used to study the interparticle contacts, particle spatial distribution and orientation, and so forth. This approach has been used in the study of gas-fluidized beds of fine spheres.[3,20] Efforts have also been made to develop this approach further to study the dynamics of ellipsoidal particles coupled with fluid flow.[22,26]

In this work, CFD–DEM is extended to fine ellipsoids for the first time. Ellipsoids with aspect ratios from 0.25 to 3.5, and size from 25 $\mu$m to 10 mm are used. The aim of the work is to investigate the effect of particle size and shape on the flow parameters, for example, minimum fluidization velocity ($U_{\mathrm{mf}}$) and minimum bubbling velocity ($U_{\mathrm{mb}}$), and explore the effect of the van der Waals force on the formation of different flow regimes.

## Model Description

CFD–DEM model for spheres has been well established and documented.[34] Its extension to ellipsoids has been demonstrated for gas fluidization.[22] For fine ellipsoids, an additional force, namely the van der Waals force, should be incorporated into the model. The following gives a brief description of the model used in this work.

### *CFD–DEM governing equations*

According to the DEM, a particle in a gas-fluidized bed can have two types of motion: translational and rotational, which are determined by Newton's second law of motion. The governing equations for the translational and rotational motion of particle $i$ with radius $R_i$, mass $m_i$, and moment of inertia $I_i$ can be written as

$$m_i\frac{d\mathbf{v}_i}{dt}=\mathbf{f}_{\mathrm{pf},i}+\sum_{j=1}^{k_c}(\mathbf{f}_{\mathrm{c},ij}+\mathbf{f}_{\mathrm{d},ij}+\mathbf{f}_{\mathrm{v},ij})+m_i\mathbf{g} \tag{1}$$

and

$$I_i\frac{d\boldsymbol{\omega}_i}{dt}=\sum_{j=1}^{k_c}(\mathbf{M}_{\mathrm{t},ij}+\mathbf{M}_{\mathrm{r},ij}+\mathbf{M}_{\mathrm{n},ij}) \tag{2}$$

where $\mathbf{v}_i$ and $\boldsymbol{\omega}_i$ are the translational and angular velocities of particles, respectively, and $k_c$ is the number of particles in interaction with particle $i$. The forces involved are: particle–fluid interaction force $\mathbf{f}_{\mathrm{pf},i}$, the gravitational force $m_i\mathbf{g}$, and interparticle forces between particles, which include elastic force $\mathbf{f}_{\mathrm{c},ij}$, and viscous damping force $\mathbf{f}_{\mathrm{d},ij}$. For fine particles, the van der Waals force $\mathbf{f}_{\mathrm{v},ij}$ needs to be considered. These interparticle forces can be resolved into the normal and tangential components at a contact point. The torque acting on particle $i$ by particle $j$ includes two components: $\mathbf{M}_{\mathrm{t},ij}$ which is generated by tangential force and causes particle $i$ to rotate, and $\mathbf{M}_{\mathrm{r},ij}$ commonly known as the rolling friction torque, is generated by asymmetric normal forces and slows down the relative rotation between particles. Additional torque $\mathbf{M}_{\mathrm{n},ij}$ should be added because the normal contact force and the van der Waals force do not necessarily pass through the particle center. A particle may undergo multiple interactions, so the individual interaction forces and torques are summed over the $k_c$ particles interacting with particle $i$.

The continuum fluid phase is calculated from the continuity and Navier–Stokes equations based on the local mean variables over a computational cell, which can be written as

$$\frac{\partial\varepsilon_{\mathrm{f}}}{\partial t}+\nabla\cdot(\varepsilon_{\mathrm{f}}\mathbf{u})=0 \tag{3}$$

$$\frac{\partial(\rho_{\mathrm{f}}\varepsilon_{\mathrm{f}}\mathrm{u})}{\partial t}+\nabla\cdot(\rho_{\mathrm{f}}\varepsilon_{\mathrm{f}}\mathrm{uu})=-\nabla p-\mathrm{F}_{\mathrm{pf}}+\nabla\cdot\varepsilon_{\mathrm{f}}\tau+\rho_{\mathrm{f}}\varepsilon_{\mathrm{f}}\mathrm{g} \tag{4}$$

where $\mathbf{u}$, $\rho_{\mathrm{f}}$, $p$ and $\mathrm{F}_{\mathrm{pf}}=(\sum_{i=1}^{k_V}\mathrm{f}_{\mathrm{pf},i})/\Delta V$ are the fluid velocity, density, pressure, and volumetric fluid–particle interaction force, respectively. Note that in this study, the particle–fluid interaction force $\mathbf{f}_{\mathrm{pf},i}$ includes drag force $\mathbf{f}_{\mathrm{d},i}$ (as shown in Table 1) and pressure gradient force $\mathbf{f}_{\nabla p,I}$ ($=-\nabla p\cdot V_i$), which usually are two dominant forces in gas fluidization. $\boldsymbol{\tau}$ and $\varepsilon_{\mathrm{f}}$ are the fluid viscous stress tensor and porosity, respectively, which are given as $\boldsymbol{\tau}=\mu_{\mathrm{e}}[(\nabla\mathbf{u})+(\nabla\mathbf{u})^{-1}]$ and $\varepsilon_{\mathrm{f}}=1-(\sum_{i=1}^{k_V}V_i)/\Delta V$, where $V_i$ is the volume of particle $i$ (or part of the volume if the particle is not fully in the CFD cell), $k_V$ is the number of particles in the CFD cell, and $\mu_{\mathrm{e}}$ the fluid

effective viscosity determined by $k$-$\varepsilon$ turbulent model,[35] which has been used in our previous work.[36] Note that the effect of gas turbulence on solid flow has been tested, and it is found that the effect can be ignored for coarse particles.[37] However, further tests are needed to justify if this treatment can be applied to fine particles.

Note that in CFD–DEM coupling, the slip velocity for the calculation of drag force is based on the velocity difference of particle velocity at a particle scale and fluid velocity at a CFD cell scale. The CFD cell size is typically set as 2–3 particle diameters. It should be pointed out that slip velocity can have three definitions based on fluid velocity[38]: interpolating the fluid velocity to the particle center, averaging the fluid velocity at the particle surface, and averaging the fluid velocity at scales larger than the particle. In the CFD–DEM, the slip velocity usually refers to the third method, and given by $U_{\text{slip}} = (\mathbf{u}_i\text{-}\mathbf{v}_i)\varepsilon_i$, where $\mathbf{v}_i$ is the particle velocity, $\mathbf{u}_i$ is the fluid velocity in the CFD cell where particle $i$ locate, and $\varepsilon_i$ is the local fluid fraction in the CFD cell.

### *Particle–particle and particle–fluid interaction forces*

*Particle–Particle Interaction Force.* Equations used to calculate the interaction forces and torques between two spheres have been well-established[32] and extended to ellipsoids.[22,39] As ellipsoidal particles have smooth/continuous surfaces like a sphere, the Coulomb condition or sliding/rolling friction models for ellipsoids are the same as for the spheres. Similarly, other important forces such as the normal and tangential contact forces, are also proven to be valid for ellipsoidal particles recently using finite element method.[40] Therefore, the force models previously formulated for spheres can be safely used in this work. The equations used to calculate the particle–particle interaction forces and torques, and particle–fluid drag force $\mathbf{f}_{\text{d},i}$ are listed in Table 1.

For fine particles, the van der Waals force should be considered. Generally, the Hamaker theory[41] is used to calculate the van der Waals force for fine spheres. Everaers and Ejtehadi[42] derived the interaction potentials through a systematic approximation of the Hamaker integral for mixtures of ellipsoids of arbitrary size and shape, namely the RE-squared potential which is a coarse-grained description of the attractive and repulsive interactions between two biaxial molecules.[43]

$$U_A = -\frac{A_{ij}}{36}\left(1+3\eta_{ij}\chi_{ij}\frac{\sigma}{h_{ij}}\right) \times\left(\frac{a_i}{a_i+h_{ij}/2}\right)\left(\frac{b_i}{b_i+h_{ij}/2}\right)\left(\frac{c_i}{c_i+h_{ij}/2}\right) \times\left(\frac{a_j}{a_j+h_{ij}/2}\right)\left(\frac{b_j}{b_j+h_{ij}/2}\right)\left(\frac{c_j}{c_j+h_{ij}/2}\right) \tag{5}$$

where $a_i$, $b_i$, and $c_i$ are the semiaxis of the ellipsoid $i$; $h_{ij}$ is the minimum surface separation. Figure 1 shows the approach of two ellipsoids. The orientation and relative position-dependent part are specified with a product of two terms

$$\eta_{ij}\chi_{ij} = \frac{2\sigma^{-1}}{\sqrt{\left(\frac{1}{R_i}-\frac{1}{R_i'}\right)\left(\frac{1}{R_j}-\frac{1}{R_j'}\right)\sin^2(\theta)+\left(\frac{1}{R_i}+\frac{1}{R_j}\right)\left(\frac{1}{R_i'}+\frac{1}{R_j'}\right)}} \tag{6}$$

where, $R_i$ and $R'_i$ are the two different principal radii of curvature at the point of closest approach, $\theta$ is the relative angle that the principal axes of the two surfaces can be rotated relative to each other, and $\sigma$ is the atomic/particle interaction radius.

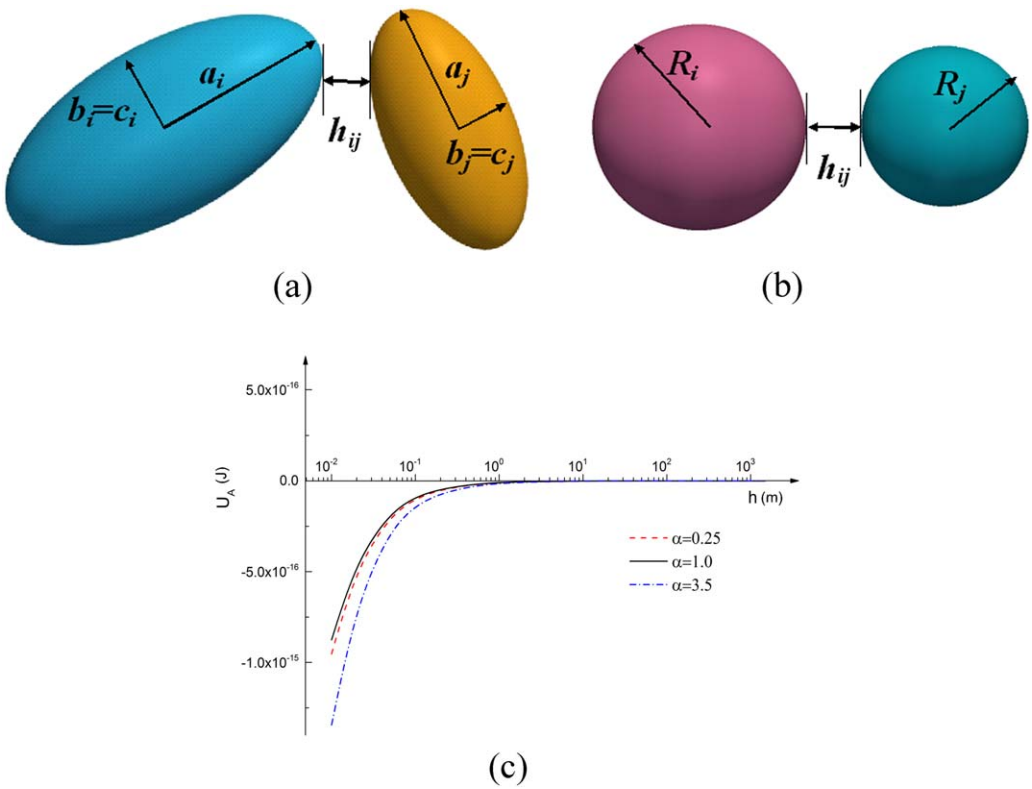


**Figure 1. Schematic of contact of two interactive spheroids (a) and spheres (b), and (c) the potential energy of ellipsoids with different aspect ratios when they are approaching with face-to-face contact.**

**[Color figure can be viewed in the online issue, which is available at wileyonlinelibrary.com.]**

The van der Waals attraction force can be obtained by differentiating interaction potential $U_A$ with regard to the minimum surface separation $h_{ij}$, which can be determine by the geometric potential detection algorithm[44,45] mentioned hereinafter. For spheroids, the expression for oblate ($a = b > c$) or prolate ($a = b < c$) particles is given as

$$f_{\mathrm{vdw}} = -\frac{A_{ij}}{12}\frac{\eta_{ij}\chi_{ij}\sigma}{{h_{ij}}^2}\left(\frac{a}{a+0.5h_{ij}}\right)^4\left(\frac{c}{c+0.5h_{ij}}\right)^2 \tag{7}$$

where $a$, $b$, and $c$ are the three principal semiaxis of the ellipsoid $i$; $h_{ij}$ is the minimum surface separation, $A_{ij}$ is the Hamaker constant, $\eta_{ij}\chi_{ij}$ is a coefficient dependent both on the orientation and relative position, and $\sigma$ is the atomic/particle interaction radius. For spheres of uniform size, the above formula reduces to

$$f_{\mathrm{vdw}} = -\frac{A_{ij}}{12}\frac{R}{{h_{ij}}^2}\left(\frac{R}{R+h_{ij}/2}\right)^6 \approx -\frac{A_{ij}R}{12{h_{ij}}^2} \tag{8}$$

In DEM simulations, particle collisions are considered to cause overlaps in colliding particles. As demonstrated in Figure1c, when the minimum separation decreases, the potential energy $U_A$ increases dramatically. Hence, a minimum separation or a cut-off distance $h_{\min}$ should be assumed to avoid a singularity in the attractive force when $h_{ij}$ equals zero. In this work, the cut-off distance is set to 1 nm as used for fine spheres by some investigators.[20,46] Additionally, a maximum cut-off is also set at a distance where the van der Waals force is far smaller than particle gravity, and over which the van der Waals forces will no longer be considered.

*Particle–Fluid Interaction Force.* Real particles can be cubes, cylinders, and ellipsoids, or more generally, irregular shapes.[47] Such morphological diversity adds further difficulties in the estimation of particle–fluid interactions. In principle, a correlation formulated for uniform spheres cannot be directly applied to those real nonspherical particles. As an alternative, they are treated as volume-equivalent spheres,[48] regardless of particle morphology. However, this simple treatment gives inaccurate results,[49] because particle–fluid interactions are strongly dependent on particle shape. Therefore, detailed information on the drag force acting on these particles is necessary for the motion of nonspherical particles. A few efforts have been made on the drag coefficient of particles of different shapes, and several drag coefficient correlations are available for nonspherical particles, for example, the Ergun,[48] Singh et al.,[50] Haider and Levenspiel,[29] Ganser,[30] Hölzer and Sommerfeld,[31] and Sommerfeld and Laín[51] correlations. Haider and Levenspiel[29] correlated experimental data on nonspherical particles by a four-parameter equation. Ganser[30] proposed a simplified drag equation which is claimed to be applicable to all shapes but valid only for $\mathrm{Re}\,K_1K_2 < 10^5$, where Re is the Reynolds number, $K_1$ is the Stokes' shape factor, and $K_2$ is the Newton's shape factor. Sommerfeld and Laín[51] found that the Ganser correlation[30] resulted in higher particle mean velocities than that of Haider and Levenspiel.[29] Hölzer and Sommerfeld[31] then established a formula for $C_D$ over a wide range of Re numbers, including high Reynolds numbers using a large number of experimental data from the literature and a comprehensive numerical study. Their expression is given by

$$C_D = \frac{8}{\mathrm{Re}}\frac{1}{\sqrt{\phi_{\parallel}}} + \frac{16}{\mathrm{Re}}\frac{1}{\sqrt{\phi}} + \frac{3}{\sqrt{\mathrm{Re}}}\frac{1}{\phi^{3/4}} + 0.4210^{0.4(-\log\Phi)^{0.2}}\frac{1}{\phi_{\perp}} \tag{9}$$

where $\phi$ is the sphericity; and $\phi_{\perp}$ is the crosswise sphericity, which is equal to the ratio between the cross-sectional area of the volume equivalent sphere and the cross-sectional area of the particle considered, perpendicular to the flow. This formula can be applied with high confidence in numerical computations as confirmed by Hilton et al.[26] As for the three models mentioned above, Zhou et al.[22] concluded that there is no significant difference between the correlation of Hölzer and Sommerfeld[31] and that of Ganser,[30] but the correlation of Haider and Levenspiel[29] significantly under-estimates the pressure drop. In this work, the Hölzer and Sommerfeld[31] model is used.

It should be noted that ellipsoidal particles can rotate by the torque caused by the nonuniform gas flow. As pointed out by Hilton et al.,[26] due to the approximately parallel flow of fluid, the rotation motion of particles caused by fluid can be neglected. For simplicity, it is thus not considered in this work.

### *Contact detection and particle orientation*

The major differences in the DEM simulation of nonspherical particles from spherical particles are the contact detection and the determination of particle orientation. The treatments used in the current model on the above two issues are briefly described below.

Various analytical methods have been proposed to detect contacts between ellipses or ellipsoids, including intersection algorithm,[52] geometric potential algorithm,[44,45] and common normal algorithm.[45] Džiugys and Peters[53] concluded that the algorithm based on the geometric potential was more favorable in terms of the accuracy and efficiency. Therefore, it has been used in most of the simulations thereafter,[22,53,54] and is also used in this work. In this algorithm, the contact location point is defined as the midpoint of the line connecting the "touch" points which are defined as the "deepest" point of ellipse $i$ (or $j$) inside ellipse $j$ (or $i$). It should be pointed out that the computational time for the contact detection is huge, which is largely because the algorithm used to determine one contact point involves the numerical solution of a sixth-order polynomial equation.

According to the Euler equations, in the three-dimensional (3-D) space, the equations of rotation can be written as

$$\begin{aligned} I_1\frac{d\boldsymbol{\omega}^b_{ix'}}{dt} - \boldsymbol{\omega}^b_{iy'}\boldsymbol{\omega}^b_{iz'}(I_2 - I_3) &= T^b_{ix'} \\ I_2\frac{d\boldsymbol{\omega}^b_{iy'}}{dt} - \boldsymbol{\omega}^b_{iz'}\boldsymbol{\omega}^b_{ix'}(I_3 - I_1) &= T^b_{iy'} \\ I_3\frac{d\boldsymbol{\omega}^b_{iz'}}{dt} - \boldsymbol{\omega}^b_{ix'}\boldsymbol{\omega}^b_{iy'}(I_1 - I_2) &= T^b_{iz'} \end{aligned} \tag{10}$$

where the inertia tensor always is diagonal $I_i = (I_{1i}, I_{2i}, I_{3i})$ in a body-fixed coordinate system (marked as superscript $b$), $\omega_i$ and $T_i$ denotes the angular velocity and torque of particle $i$. For 3-D particles, the moments of inertia $I_i$ must be calculated in every time step according to the new orientation of the particle in the space. For spherical particles, $I_{1i} = I_{2i} = I_{3i} = I_i$ and body-fixed coordinates can be set in the same direction as space-fixed ones. For nonspherical particles, the local and global orientation of the particle can be transformed using

**Table 2. Parameters Used in the CFD–DEM Simulations**

| Parameters | Value |
|---|---|
| Particle size ($d_p$), $\mu$m | 25, 50, 100, 500, 1000, and 10,000 |
| Particle density ($\rho_p$), kg/m$^3$ | 1349.5 |
| Particle shape | Oblate, spherical, and prolate |
| Particle aspect ratio ($\alpha$) | 0.25, 0.5, 0.75, 1.0, 1.5, 2.5, 3.0, and 3.5 |
| Number of particles ($N$) | 18,000 |
| Fluid density ($\rho_g$), kg/m$^3$ | 1.205 |
| Bed size (width $\times$ thickness $\times$ height), $d_p$ | 60 $\times$ 6 $\times$ 480 |
| Number of CFD cells | 20 $\times$ 160 |
| Young's modulus ($Y$), N m$^2$ | 1.0 $\times$ 10$^7$ |
| Poisson's ratio ($v$) | 0.30 |
| Friction coefficient ($\mu$) | 0.3 |
| Normal damping coefficient ($c_n$) | 0.3 |
| Hamaker constant ($H_a$), J | 0, 2.1 $\times$ 10$^{-21}$(default), 4.2 $\times$ 10$^{-21}$ |
| Cut off distance ($h_{min}$), nm | 1 |
| Time step ($\Delta t$), s | 1 $\times$ 10$^{-6}$~5 $\times$ 10$^{-5}$ |

two, namely, the space-fixed and body-fixed coordinate systems. The space-fixed coordinate system is fixed with respect to the laboratory space. Conversely, the body-fixed (or local) coordinate system is a moving Cartesian coordinate system, which is fixed with respect to the particle and the axes are superimposed by the principal axes of inertia.[55] Any vector can be transformed from the space-fixed axes into the body-fixed axes and vice versa via a transformation matrix which can be expressed by the quaternion method.[30,56] More details can be found elsewhere.[53,57]

### *Coupling scheme*

The CFD–DEM coupling methodology for spherical particles[32,58,59] has been extended to nonspherical particles.[22] It is used in this work. Thus, at each time step, DEM will give information such as the positions and velocities of individual particles. From these information, the porosity and volumetric fluid–particle interaction force in each computational cell are calculated. CFD will then use the information to determine the gas flow field, from which the fluid drag forces acting on individual particles are calculated. Incorporation of the resulting forces into DEM will produce information on the motion of the individual particles for the next time step.

## Simulation Conditions

Table 2 lists the settings of the bed and particle properties used in the simulation cases. In DEM model, walls are assumed to have the same properties as particles. The coupled approach of 3-D DEM and 2-D CFD, which has been widely used in our previous studies,[22,59] is adopted in this work. The flow of gas is assumed to be 2-D, given that the bed width is much larger than its thickness. Hence, there is no boundary condition for gas flow in the front–rear direction. For particles, periodical boundary conditions are applied along the front and rear directions as they have been recognized as the most useful treatment to eliminate the effects of front and rear walls and, at the same time, can maintain a continuous internal flow involving particle–particle contacts throughout the computational domain.[60]

Singh et al.[16] showed that for a specific column diameter or bed width, the static bed height has slight effect on minimum bubbling velocity. Wang et al.[11] found that minimum bubbling velocities (determined by the bed contraction phenomenon) converge to a constant value when the number of particles exceeds a certain value. Considering the high computational effort for low aspect ratio (e.g., aspect ratio = 0.25) or high aspect ratio (e.g., aspect ratio >2.5), which may be 5–7 times slower than spheres, 18,000 particles are used in this work, and they can form a packed bed with an acceptable height. Packing methods such as poured packing and random packing are usually used to form packed beds. We compared the bed porosity for both methods, and little difference is found. But note that for random packing, a very high bed is often needed to avoid particle overlap in the initial state. Therefore, the poured packing method is used to generate the packed beds in this work. The simulation begins with the pouring of mono-sized and mono-shaped ellipsoidal particles into a rectangular box. When all particles have reached their stable positions with an essentially zero velocity, gas is introduced from the bed bottom at a fixed velocity. The fluidization process is considered to have reached the pseudostable state when the particles velocities and the average coordinate numbers fluctuate around fixed values.

Spheroids with aspect ratios varying from 0.25 to 3.5 are used in this work to produce shapes from oblate to prolate spheroids. Spheroids have three principal diameters. Let $a$ be the principal radius in the polar direction, and $b$ and $c$ the principal radii in the equatorial plane. Here, the particle shape factor, namely aspect ratio $\alpha$ is defined as, $\alpha = c/a$. For a prolate ($a > b = c$) spheroid, aspect ratio $\alpha > 1$; for a sphere ($a = b = c$), $\alpha = 1$; and for an oblate ($a = b > c$) spheroid, $\alpha < 1$. The Hamaker constant is in the range from 0 to 4.2 $\times$ 10$^{-21}$ J. Unless otherwise specified, it is set to 2.1 $\times$ 10$^{-21}$ J.

For the same particle size, aspect ratio can significantly affect fluidization parameters, for example, minimum fluidization velocity $U_{mf}$ and minimum bubbling velocity $U_{mb}$. Hence, it is not suitable to use the same gas velocity $U_g$ to study the effect of aspect ratio on flow behavior. To overcome this problem, we use a comparable gas velocity condition in this work, for example, 0.5 $U_{mb}$ for expanded beds and 2 $U_{mb}$ for fluidized beds. For the particle size of 50 μm, the corresponding $U_{mb}$ for the nine aspect ratios listed in Table 2 are 0.02, 0.013, 0.011, 0.01, 0.013, 0.015, 0.0175, 0.0195, and 0.021 m/s, respectively.

The in-house CFD–DEM code is used in this work, and all simulations are run in the National Computing Infrastructure (NCI) in Australia. As the computation involves the numerical solution of a sixth-order polynomial equation for ellipsoids,

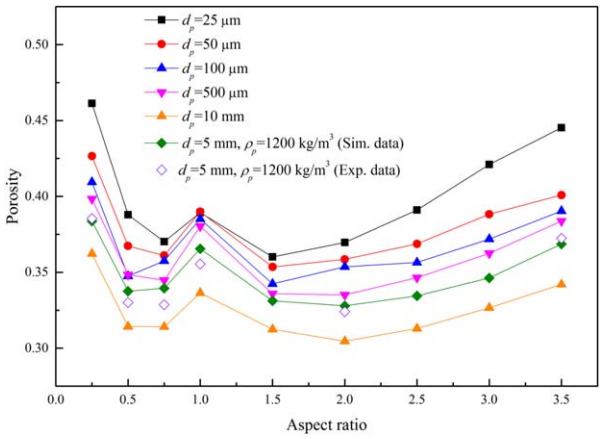


**Figure 2. Effects of particle size and shape on porosity in packed beds.**

**[Color figure can be viewed in the online issue, which is available at wileyonlinelibrary.com.]**

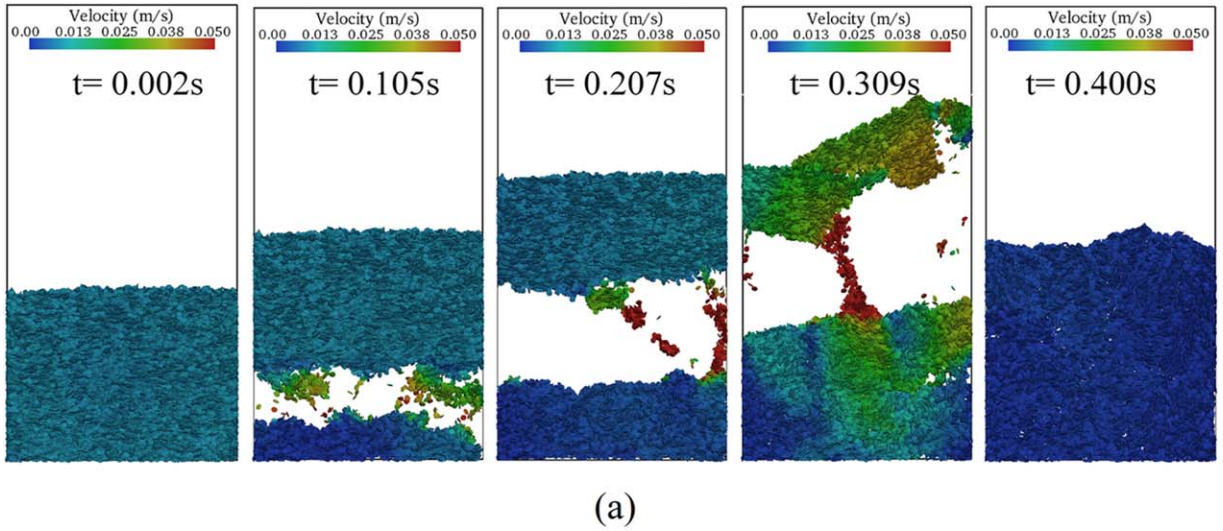


(a)

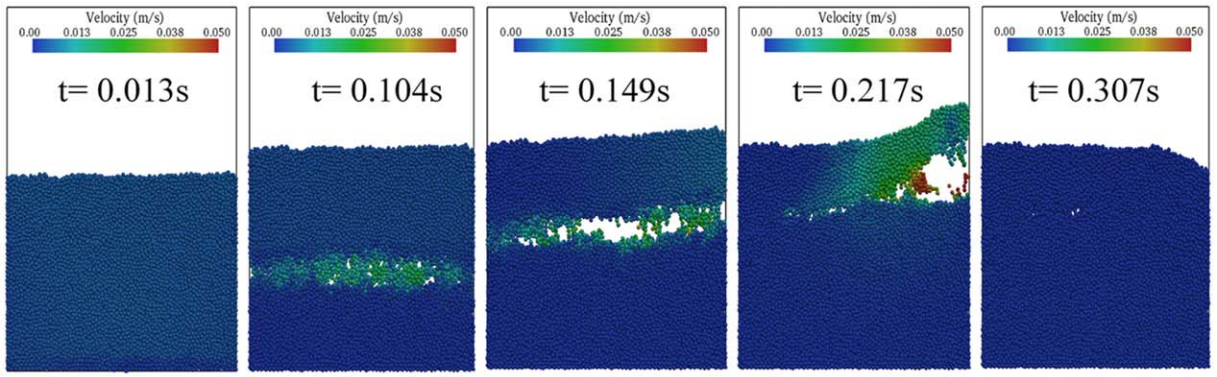


(b)

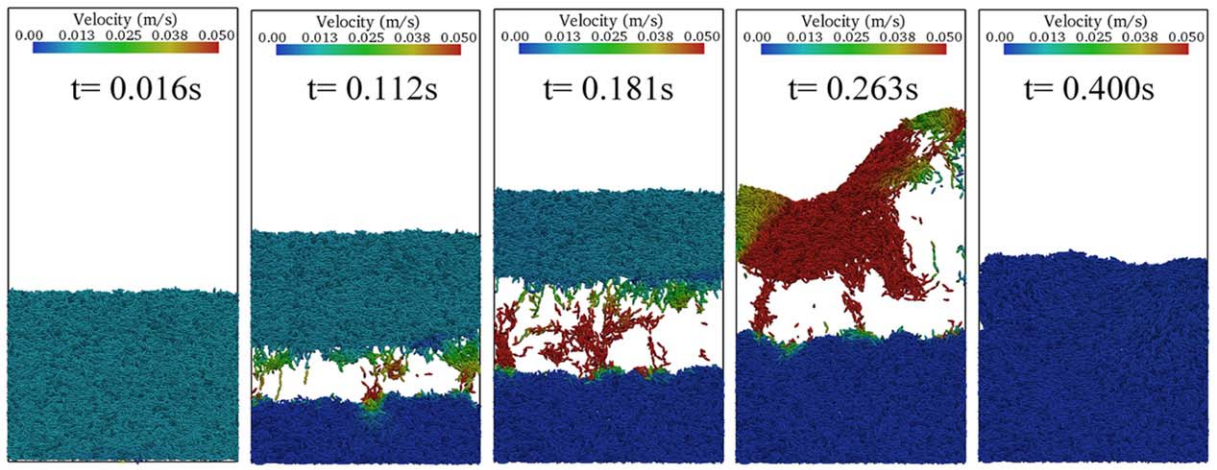


(c)

**Figure 3. Snapshots of flow patterns in the formation of expanded beds of group-A powders [$d_p$ = 50 μm, $U_g$ = 0.5 $U_{mb}$, (a) $\alpha = 0.25$, (b) $\alpha = 1.0$, and (c) $\alpha = 3.5$, colored by particle velocity].**

**[Color figure can be viewed in the online issue, which is available at wileyonlinelibrary.com.]**

and small time steps for fine particles, the time required to complete one case simulation varies from several days to 1 or 2 months, depending on the particle size and aspect ratio. The smaller the particle sizes or the more nonspherical the particles are, the longer the computational time.

## Results and Discussion

### *Packing properties*

Fluidization behavior such as minimum fluidization velocity is closely associated with the initial packing structure, the

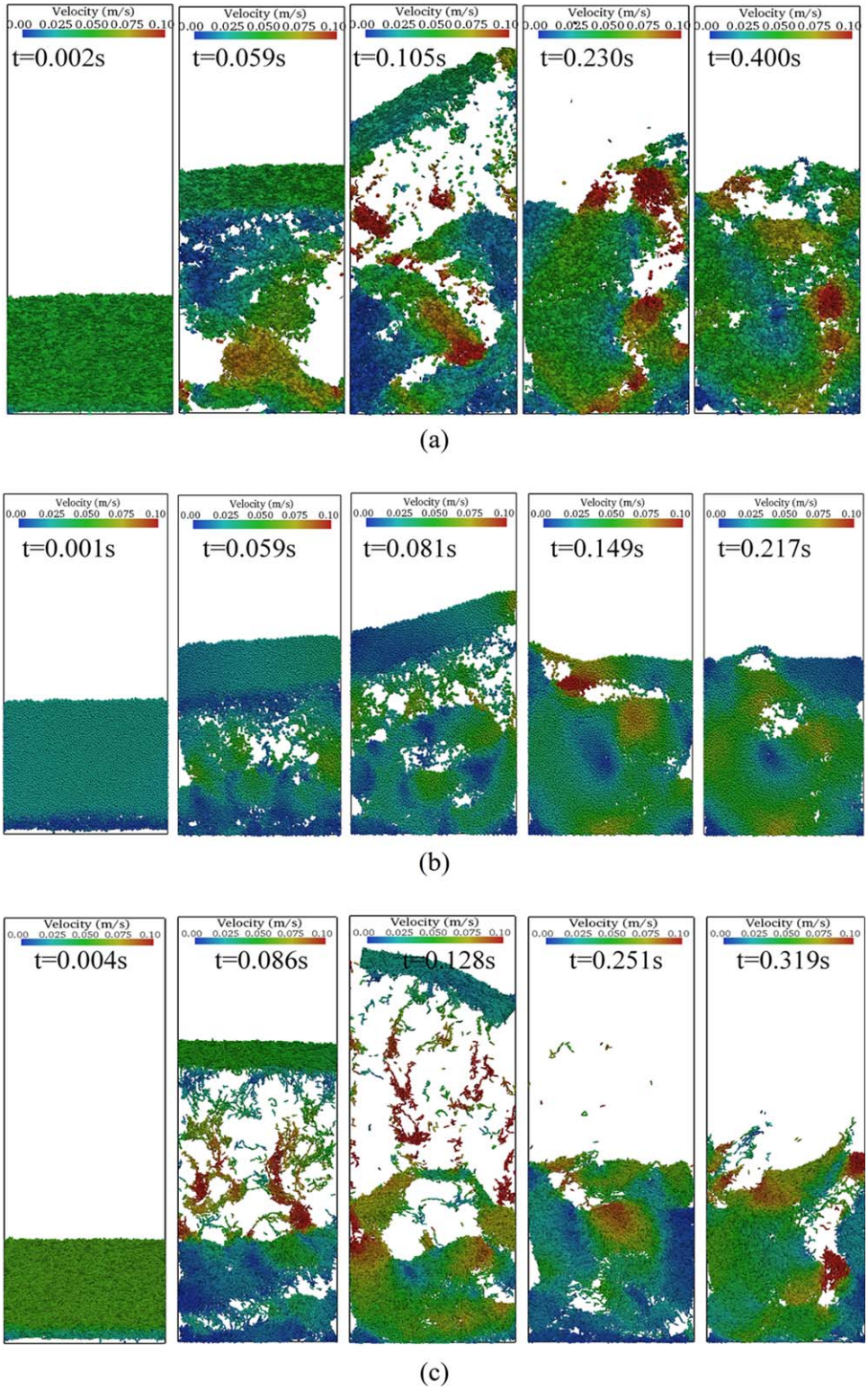


**Figure 4. The snapshots of the simulation results of the macro-fluidization for different particle shape [$d_p$ = 50 μm, $U_g$ = 2 $U_{mb}$, (a) $\alpha = 0.25$, (b) $\alpha = 1.0$, and (c) $\alpha = 3.5$, colored by particle velocity].**

**[Color figure can be viewed in the online issue, which is available at wileyonlinelibrary.com.]**

porosity in particular. The effect of particle aspect ratio on bed porosity of different particle diameter $d_p$ is examined, and the results are shown in Figure 2. It can be seen that the porosity shows a W-shaped variation with aspect ratio for different particle sizes. The lowest porosities occur when aspect ratio is around 0.75 for oblate spheroids and 1.5 for prolate spheroids. These results are consistent with those reported in the literature for ellipsoids and spherocylinders.[39,61,62] Williams and Philipse[62] explained that the packing porosity is the combined effect of coordination numbers determined by local caging effects and excluded volumes effects. For nearly spherical particles, the excluded volume depends weakly on aspect ratio.

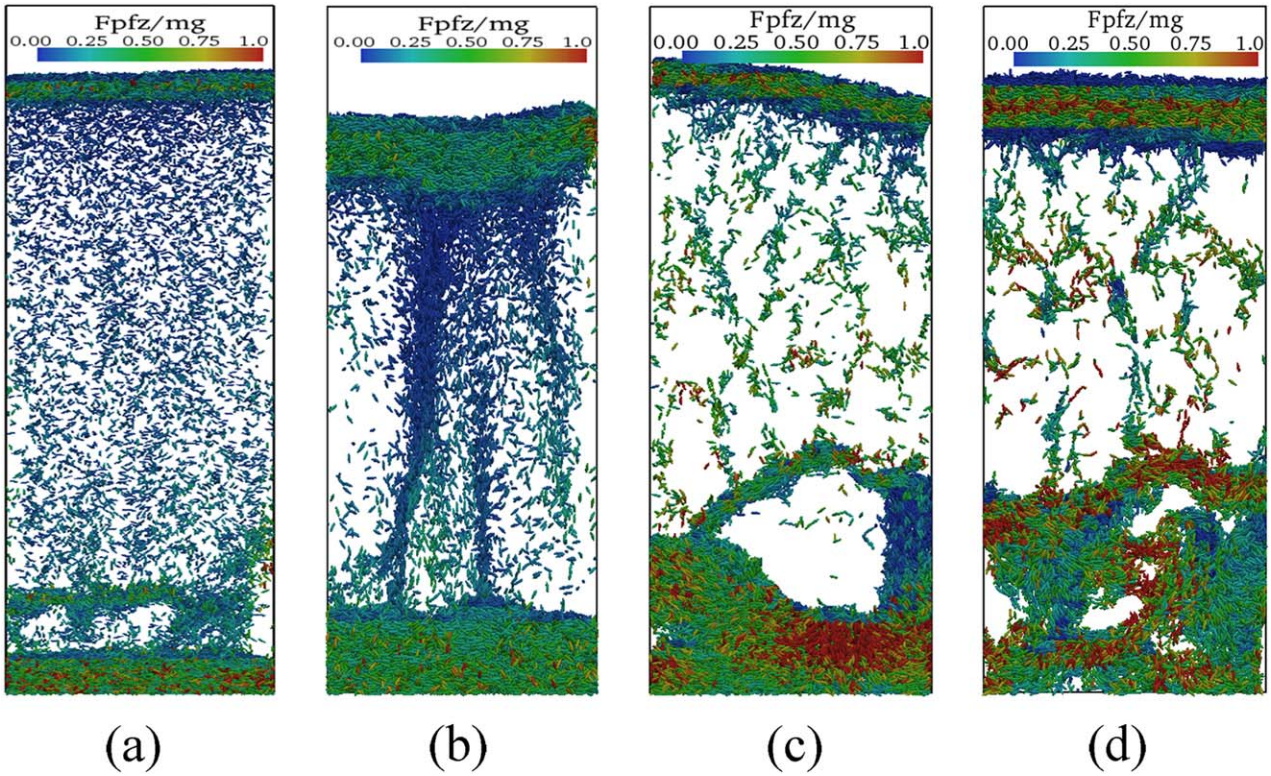


**Figure 5. The snapshots of the simulation results of the flow patterns for prolate particles with different particle sizes [$\alpha = 3.5$, $U_g = 2\ U_{mb}$, (a) $d_p = 1000$ μm, $t = 0.698$ s, (b) $d_p = 500$ μm, $t = 0.156$ s, (c) $d_p = 100$ μm, $t = 0.160$ s, and (d) $d_p = 50$ μm, $t = 0.098$ s, colored by particle-fluid force in $z$ direction/gravity ($F_{pfz}$/mg)].**

**[Color figure can be viewed in the online issue, which is available at wileyonlinelibrary.com.]**

With aspect ratio deviating from 1.0, a large number of contacts are required to cage ellipsoids, causing porosity decreasing. The porosity reaches the minimum at aspect ratios of 0.75 and 1.5. Further, as particles become more flat or elongated, more contacts are required to cage particles, but meanwhile the excluded volume effect gradually becomes dominant. Thus, the intercompetition between these two effects drives the porosity to increase.

Meanwhile, when particle size reduces, the lowest porosity position changes from 0.5 to 0.75 for oblate spheroids and from 2.0 to 1.5 for prolate spheroids, and the porosity difference between spheres and ellipsoids becomes larger. The former is mainly caused by the increased role of the van der Waals force in force balance in packed beds, and the latter is caused by the difference in the van der Waals force for different aspect ratios with the same particle size. To further validate the simulated data, some laboratory experiments were also performed in this work using acrylic ellipsoidal materials with $d_p = 5$ mm. It was found that the simulated results agree well with the experimental data. Moreover, when particle size becomes smaller, the porosity increases gradually, indicating that the beds become more loosely packed.

### *Flow patterns*

Geldart A particles are characterized by the presence of bed expansion before the onset of fluidization. Figure 3 shows the formation of expanded beds for ellipsoidal particles with different aspect ratios. It can be observed that for ellipsoids with aspect ratios of 0.25 and 3.5 (Figures 3a, c), with the gas introduction into the bed, the bulk disconnects into two major parts with the upper part ascending, and the lower part falling downward due to gravity. During this process, the particles at the bottom of the upper part descend when the particle–fluid force cannot balance the bed weight. Thus, in this expanding process, the orientation of bottom part does not change much, while particles in the upper part may undergo an orientation rearrangement due to the large space between two parts during the lifting and descending process. This could give rise to the formation of more particle interlocks, which consequently results in the higher minimum bubbling velocities for nonspherical particles. Interestingly, the prolate particles shown in Figure 3c flow one after another like "chains" in the descending process. For spherical particles, however, the expanding process is relatively mild and homogeneous. The bed becomes loose and then dense again, and no obvious disconnection occurs during the expanding process, consistent with the previous study.[20] The expanding process for spheres is more stable than that for ellipsoids. This is because spheres have lower van der Waals forces than ellipsoids for the same surface separation distance or during contact as shown by the smaller potential energy in Figure 1c. Thus, the cohesion between agglomerates are easier to breakup by the contact force or particle–fluid interaction force. With the superficial gas velocity increasing, for example, above the minimum bubbling velocity, the beds become fluidized. Figure 4 shows snapshots of flow patterns when gas velocity $U_g = 2\ U_{mb}$ and particle diameter $d_p = 50$ μm. For ellipsoidal particles (Figures 4a, c), they are piled up at the beginning; the symmetric major axis is oriented vertical for oblate and horizontal for prolate particles.[22] As a result, all the particles are lifted as a bulk with the introduction of gas, and then descend due to the gravity. After the initial response, the fluidization gradually becomes steady

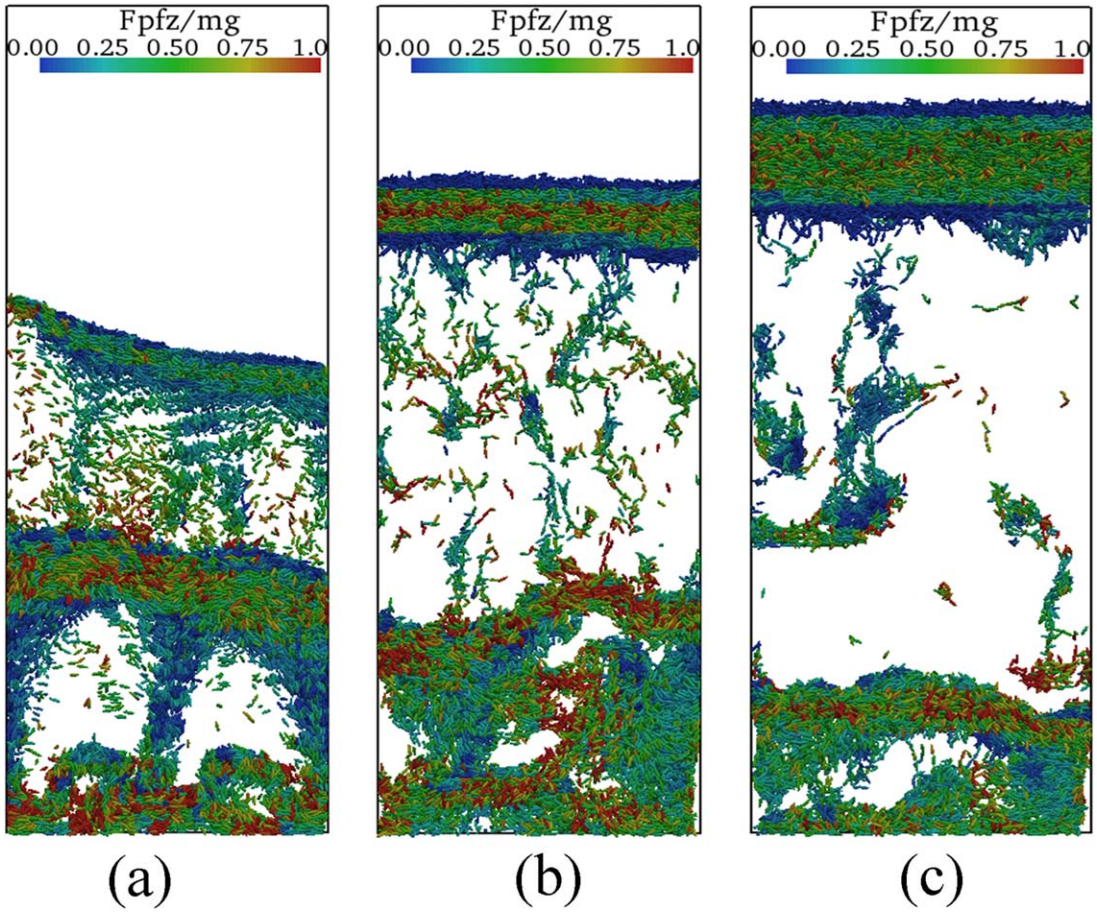


**Figure 6. The snapshots of the simulation results of the macro-fluidization for prolate particles with different Hamaker constant [$d_p$ = 50 μm, $U_g$ = 2 $U_{mb}$, $\alpha$ = 3.5, $t$ = 0.1261 s, (a) $H_a$ = 0, (b) $H_a$ = 2.1 × $10^{-21}$ J, and (c) $H_a$ = 4.2 × $10^{-21}$ J, colored by particle-fluid interaction force in $z$ direction ($F_{pfz}$/mg)].**

**[Color figure can be viewed in the online issue, which is available at wileyonlinelibrary.com.]**

with formation of various agglomerates. For spheres (Figure 4b), all the particles are lifted up and descend more particulately but continuously. Moreover, particle velocities vary significantly with time, space, and aspect ratio. For example, low particle velocities are found in the left or right corners at the bed bottom. Spheres have lower velocities than ellipsoids. In the fluidized beds of fine particles shown in Figure 4, agglomerates are formed and their shapes change with time and space. The agglomerate shapes can be cotton-shaped, ear of wheat-shaped, and strip- or chain-shaped, which are reported in literature as long frill or cluster chain,[63] vertical sheets,[64] and vertical elongated structure.[65] There are also reports of other agglomerate shapes, such as parabolic geometrical shape.[63,66] One interesting phenomenon, known as the "chain phenomenon" as mentioned earlier for expanded beds of prolate particles, can be further observed clearly in fluidized beds, as shown in Figure 4c. The prolate particles descend one after another to form chains. Essentially, these "chains" can be regarded as special shaped of agglomerates. Consistent with the elongate agglomerate shapes reported, most of the chains are found in the vertical directions (fluid velocity direction). This indicates that the fine prolate particles tend to be in head-to-head contact in fluidized beds. Further examination on the fluidization of prolate particles and related chain phenomenon is made and presented below.

It is well known that coarse particles display smooth fluidization. With the particle size decreasing, the van der Waals force becomes more important when compared with particle weight, causing formation of agglomerates, especially for prolate particles as shown in Figures 2 and 3. The effect of particle size on the flow patterns of prolate particles is shown in Figure 5. Generally, there are two typical fluidization types, particulate fluidization where particles flow individually and aggregative fluidization where agglomerates or clusters occur, varying temporarily and spatially. As expected, the flow patterns transit from particulate to aggregative fluidization when the particle size reduces from 1000 to 50 μm. More specifically, for particle size larger than 500 μm, particle flow is quite granular. But when particle size reduces to 100 μm, small agglomerates are formed. Most agglomerates are irregular bunchy in the vertical direction. Some branches of these agglomerates disappear and evolve into "chains" when particle size further decreases to 50 μm. Therefore, fine cohesive powders often have a poor fluidization quality. This will be further quantified by a fluidization index ($U_{mb}/U_{mf}$) hereinafter. Moreover, from the ratio of vertical component of particle–fluid interaction force and particle gravity, it can be observed that the vertical component of particle–fluid interaction force increases when particle size reduces. This implies that fine particles tend to flow in the vertical direction.

As mentioned in the description of Figure 5, the van der Waals force has a significant influence on the formation of agglomerates, but this influence is related to particle size, which is coupled with other variables. Thus, to eliminate the

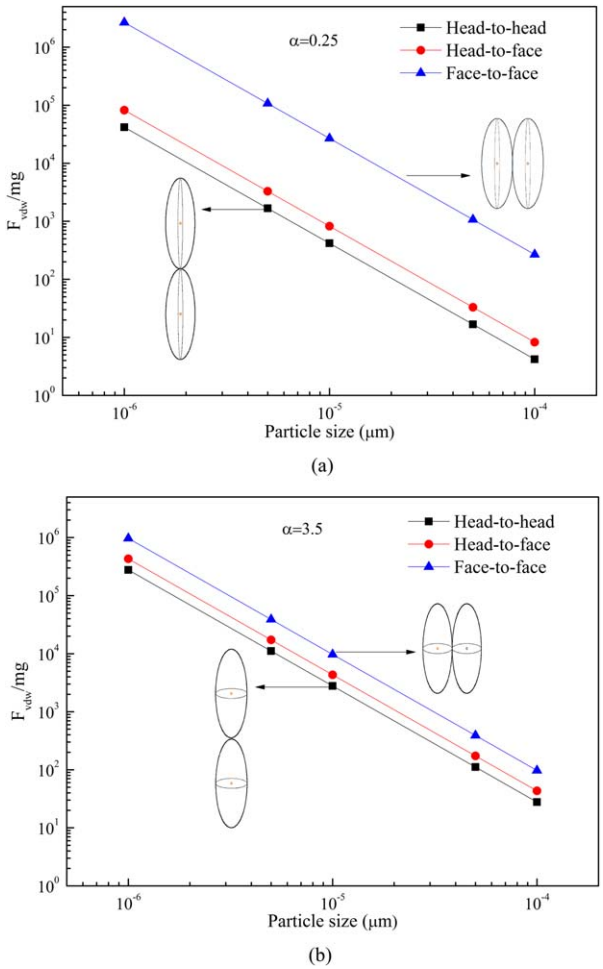


**Figure 7. Variation of the van der Waals force as a function of particle size for (a) oblate and (b) prolate particles with different contact modes.**

**[Color figure can be viewed in the online issue, which is available at wileyonlinelibrary.com.]**

coupled influence, the effect of Hamaker constant is here studied for the same particle size. As shown in Figure 6, without the van der Waals force, particles fluidize particulately. With a lower van der Waals force, particles flow in short "chains." When the Hamaker constant increases, the "chains" become longer, indicating that the van der Waals force is an essential condition to generate the "chain phenomenon."

Figure 7 shows the variation of the scaled van der Waals force as a function of particle size with different contact modes. It can be observed that for oblate particles, the scaled van der Waals force is much higher for the face-to-face contacts than for the head-to-head contacts (Figure 7a). But for prolate particles, the difference in the scaled van der Waals force between different contact modes is relative small as shown in Figure 7b. So, under the action of particle–fluid interaction force, the face-to-face contact can be easily dragged to head-to-head contact for prolate particles, but it is much difficult for oblate particles to do so.

To investigate the formation of chains, the directions of velocities of particles in different chains are shown in Figure 8. As expected, the velocities of the particles in a chain are largely in the same direction enabling particles to remain in the chains. Otherwise, the particles will be dragged away from the chain causing the chain breakage. Furthermore, from the viewpoint of the particle coordination number which is defined as the number of contacting or touching neighbors per particle, it can be found that for some particles in the chains, the coordination number is equal to 0. That is, these particles are only in close proximity but not in contact with neighboring particles, and therefore, the bond between particles in the chains is only via the van der Waals force at the particle heads in the chains.

Based on the above analysis, there are several necessary conditions to form "chains." First, the van der Waals force should be large enough; second, particles are in special shape, such as elongated shape; third, the particle velocities are largely in the same directions; last, but not least, there should be enough void to form chains. Therefore, chains are easier to be formed in the start-up stage of the fluidization process where particles are separated into two parts, and there are large voids in between them.

### *Fluidization parameters*

*Pressure Drop.* Pressure drop is an important fluidization parameter to characterize the macro flow behavior, and can be measured or predicted by experimental and simulation methods. The fluctuation of pressure drop is closely related to the behavior of particles and fluid in a bed. Figure 9 shows the variation of pressure drop with time in expanded and fluidized beds. As seen from Figure 9a, in the expanded bed, there is an obvious pressure drop fluctuation before the pressure drop levels off at the bed weight. At the beginning, the bed pressure-drop only slightly reduces as gas needs time to permeate and loosen the particle ensemble, and break the interlocks among particles. With gas permeating through the bed, some top particles are lifted before gas would have time to break all the interlocks at the top. Therefore, top particles are broken away

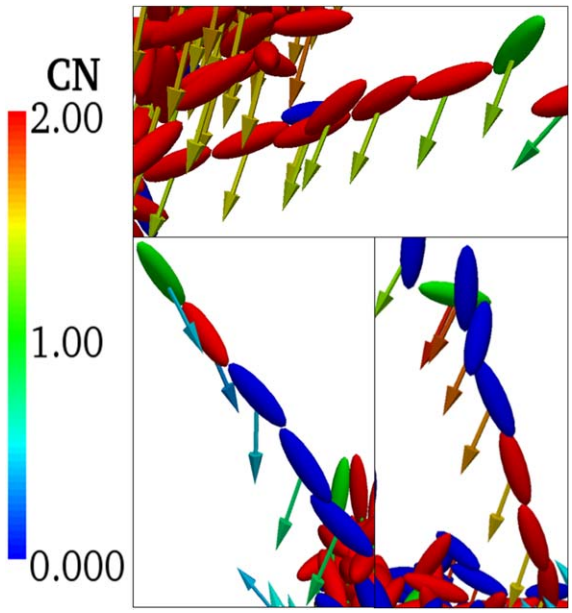


**Figure 8. Velocity directions of particles in "chains" in fluidized beds when $d_p = 50$ μm and $\alpha = 3.5$ (particles are colored by coordination number, and velocity vectors are colored by velocity magnitude).**

**[Color figure can be viewed in the online issue, which is available at wileyonlinelibrary.com.]**

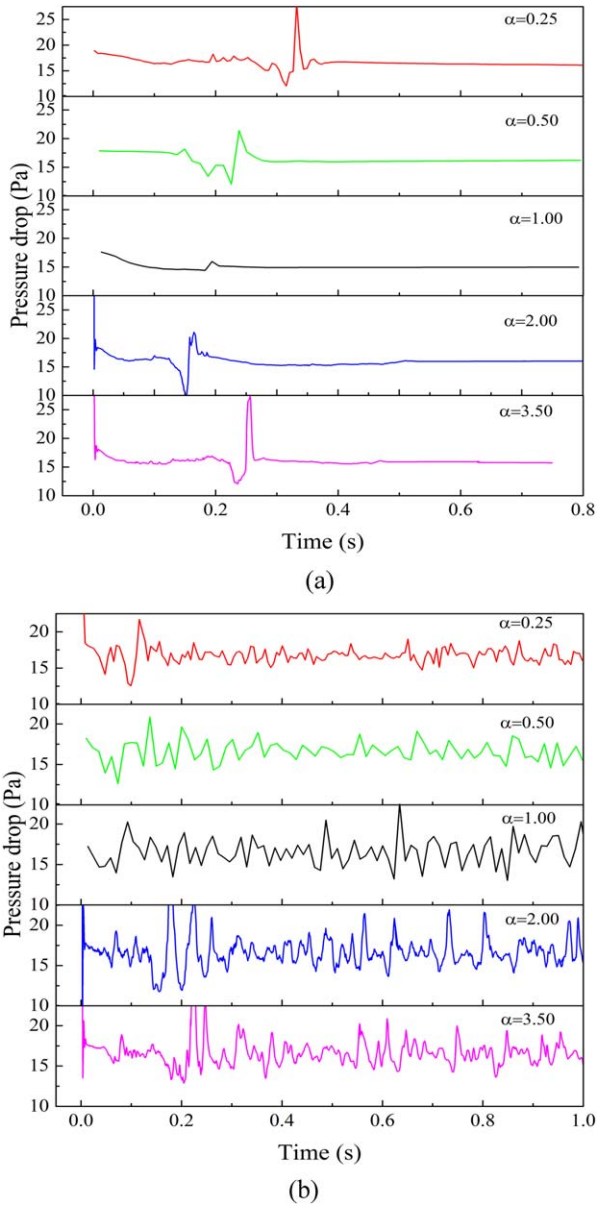


**Figure 9. Pressure drop as a function of time for different aspect ratios [$d_p$ = 50 μm, (a) $U_g$ = 0.5 $U_{mb}$ and (b) $U_g$ = 2 $U_{mb}$].**

**[Color figure can be viewed in the online issue, which is available at wileyonlinelibrary.com.]**

from the bottom ones, which leads to a marked drop in the bed pressure. When the top particles fall down with some acceleration, it adds some impact pressure to the bottom. As a result, the pressure drop suddenly increases to a level higher than the average value (bed weight). When particles become more flat or elongated, the fluctuation amplitude increases, indicating that the "impact effect" becomes more obvious. The larger fluctuation of pressure drop for ellipsoidal particles is mainly because ellipsoids tend to form large fracture in the expanding process, with the upper bulk being lifted much higher than spheres, as shown in Figure 2. Thus, when falling and reaching the bottom, they have higher velocities than spheres, and generate severer impaction on the bottom bulk. In addition, when aspect ratio deviates from 1.0, the occurrence time of the fluctuation becomes longer. This may result from the initial porosity and interlocks. Once the top particles fall down, the bed pressure drop becomes stable again. In fluidized beds (Figure 9b), after the severe turbulence at the beginning, the pressure drop fluctuates with time around a fixed number (bed weight), and the fluctuation amplitude slightly increases with aspect ratio.

The fluctuations of pressure drop across a fluidized bed are known to increase with an increase in the bubbling intensity. Figure 10 plots the variation of scaled pressure drop (=pressure drop/bed weight) with time for different particle sizes when gas superficial velocity is at 2 $U_{mb}$. For both oblate and prolate particles, the fluctuation amplitude of pressure drop grows with particle size. Similar results are found for spherical particles which are not shown here. These results are consistent with the experimental results of spherical

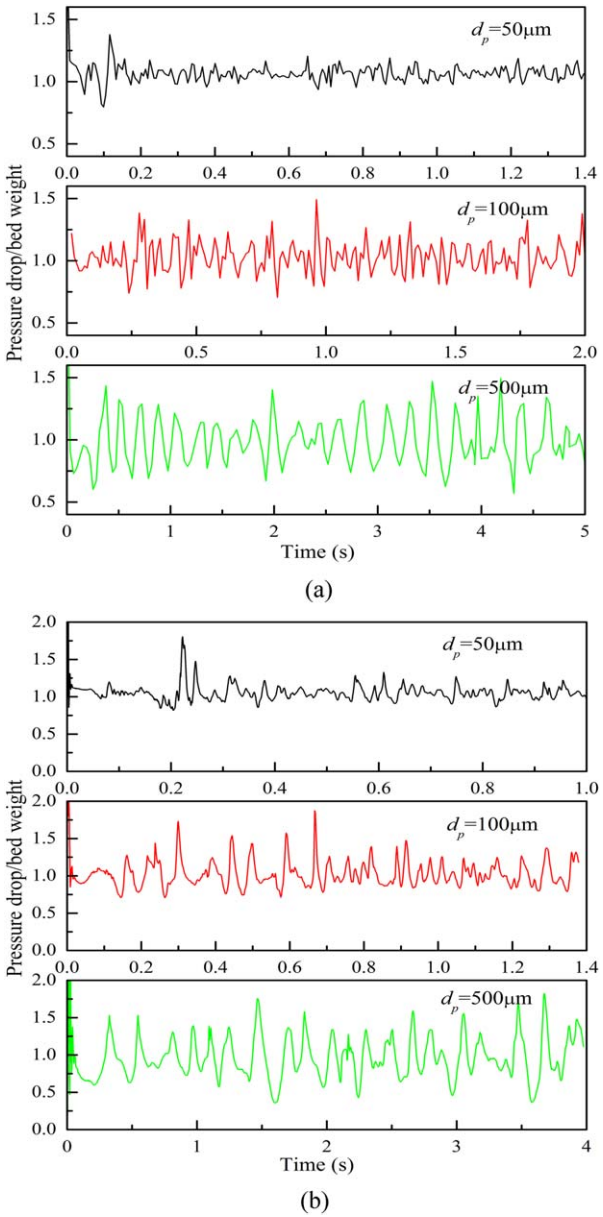


**Figure 10. Pressure drop as a function of time for different particle size [$U_g$ = 2 $U_{mb}$, (a) $\alpha = 0.25$ and (b) $\alpha = 3.5$].**

**[Color figure can be viewed in the online issue, which is available at wileyonlinelibrary.com.]**

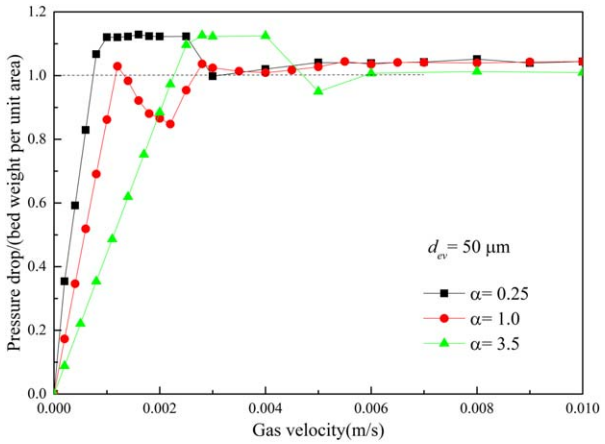


**Figure 11. Pressure drop–velocity curves for different particle sizes and aspect ratios [(a) $d_p$ = 50 μm and (b) $d_p$ = 1 mm].**

**[Color figure can be viewed in the online issue, which is available at wileyonlinelibrary.com.]**

particles.[67] This implies the increase of bubbling intensity with particle size in the fluidized flow regime.

The variation of pressure drop with gas velocity reflects the permeability of fixed beds, and can also indicate the demarcation of flow regimes. As illustrated in Figure 11, for particles with different shapes and sizes, the pressure drop–gas velocity curves vary significantly. For fine particles (Figure 11a), the bed pressure drop initially increases to a peak as the particle–fluid interaction force has to be high enough to break down the interlocking within the bed. Then, the pressure drop reduces to the bed weight per unit area or even less due to the occurrence of bed partial collapse.[68] After the fluctuation, the pressure drop finally reaches a relatively stable state at a pressure equal to the weight of the bed per unit area as the bed reaches the expanded and fluidized bed regimes. For coarse particles (Figure 11b), the pressure drop becomes stable when the pressure drop reaches the bed weight per unit area, and no significant pressure drop fluctuation occurs before fluidization. It can be seen that in fixed beds at the same gas velocity, the prolate particles have the lowest pressure drop thus the highest bed permeability. This is true for both particle sizes. The permeability is closely related to the initial bed porosity and the void connectivity. Although oblate particles have highest porosity, lowest permeability is predicted; and spherical and prolate particles with $\alpha = 3.5$ have similar initial bed porosities, but prolate particles show better permeability. This is probably because oblate particles can easily form closed voids due to being wrapped by disc faces, while prolate particles tend to form more open voids.

*Minimum Fluidization Velocity.* The minimum fluidization velocity ($U_{mf}$) is generally defined as the minimum gas velocity at which the pressure drop through the bed is equal to the bed weight per unit bed cross-section area. Below the minimum fluidization velocity, the gas will permeate although channels between particles. The magnitude of $U_{mf}$ can be determined based on the relationship between pressure drop and gas superficial velocity shown in Figure 11.

Figure 12 shows the minimum fluidization velocity for different aspect ratios and particle sizes. It can be seen that the minimum fluidization velocity increases exponentially with the increase of particle size. The predicted results agree well with the correlation of Baeyens and Geldart[69] for three particle shapes. However, for a certain particle size, the $U_{mf}$ of oblate particles are the lowest, and prolate particles the highest, except for coarse particles. This indicates that oblate particles are easier to be fluidized than spheres. One possible reason is that oblate particles can fly-like Frisbees in the fluidized bed.[70] Conversely, prolate particles have higher $U_{mf}$ because elongated particles are easy to form interlocks which hinder particle movement.

Figure 13 shows the effect of aspect ratio on the minimum fluidization velocities. As illustrated in the figure, the $U_{mf}$-aspect ratio curves largely show a "W" shape, but there are some differences for different particle sizes. For coarse particles, the two wings of the "W" are quite flat (Figures 13a, b), and even moved downwards for coarse oblate particles (Figure 13a). The predicted results are compared with the experimental data using coarse acrylic ellipsoidal materials (see Figure 13a), showing a good agreement. This tendency is also consistent with that of Zhou et al.[22] However, with the particle size decreasing, the wings of the "W" become upturned. For example, for the very fine powders of diameter 25 μm (Figure 13d), the $U_{mf}$ of prolate particles with aspect ratio larger than 2.0 are much higher than near-spherical and oblate particles. This is because that prolate particles have higher van der Waals force than spheres at the same surface separation

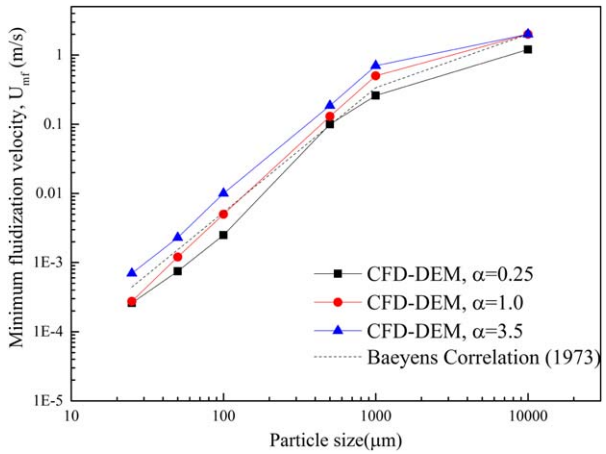


**Figure 12. Effect of particle size on the minimum fluidization velocities ($U_{mf}$).**

**[Color figure can be viewed in the online issue, which is available at wileyonlinelibrary.com.]**

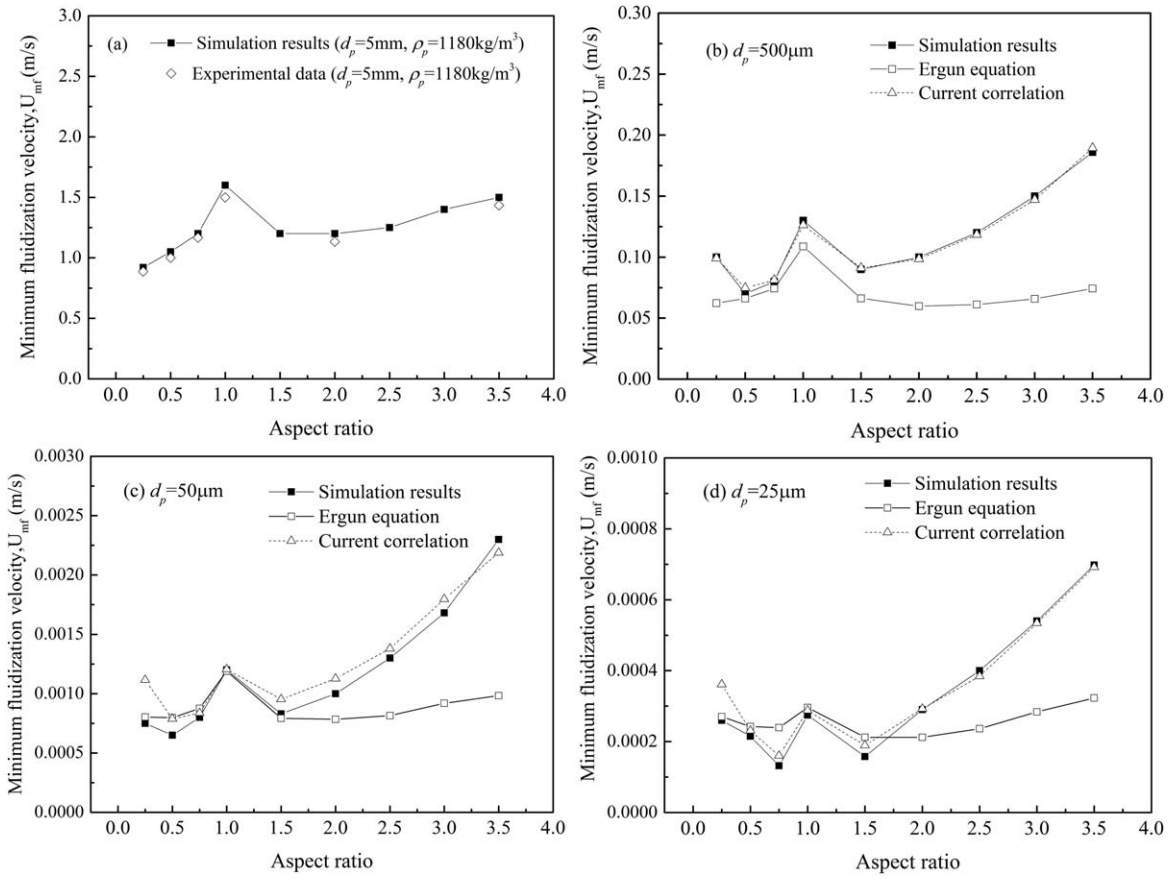


**Figure 13. Effect of particle shape on the minimum fluidization velocities ($U_{mf}$) [(a) $d_p = 5$ mm, (b) $d_p = 500$ μm, (c) $d_p = 50$ μm, and (d) $d_p = 25$ μm].**

distance or in contact (see Figure 1c). Also, prolate particles tend to form interlocks in the packed bed, which requires higher velocity to break. There are two obvious cusps at $\alpha = 0.75$ for oblate and $\alpha = 1.5$ for prolate spheroids. This is closely related to the initial porosity which also shows a "W" shape with aspect ratio, as shown in Figure 2.

There are a number of correlations to predict $U_{mf}$, as summarized by Suksankraisorn et al.[19] In these correlations, the minimum fluidization velocity is a function of the particle density, size, fluid density, and viscosity. However, only a few of these correlations include the effect of particle shape (aspect ratio or sphericity). The Ergun equation[48] is one of the few correlations that link minimum fluidization void fraction, $\varepsilon_{mf}$, to particle sphericity, $\phi$. However, it can be seen from Figure 13 that the Ergun equation cannot predict $U_{mf}$ well for ellipsoids, especially for prolate particles. Therefore, the modification is made in this work based on the Ergun equation. Aspect

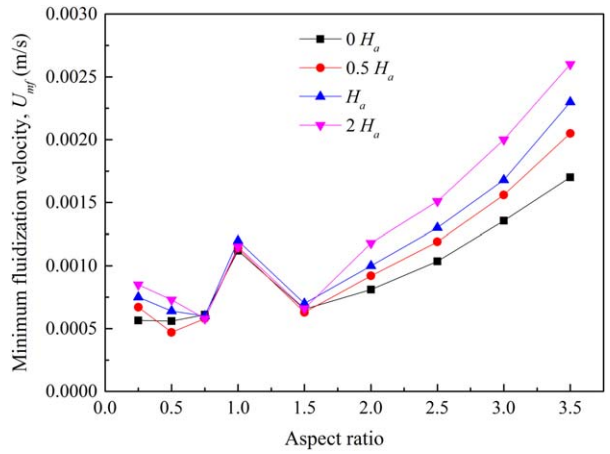


**Figure 14. Effect of Hamaker constant ($H_a$) on minimum fluidization velocity ($U_{mf}$) for different aspect ratios ($H_a = 2.1 \times 10^{-21}$ J).**

**[Color figure can be viewed in the online issue, which is available at wileyonlinelibrary.com.]**

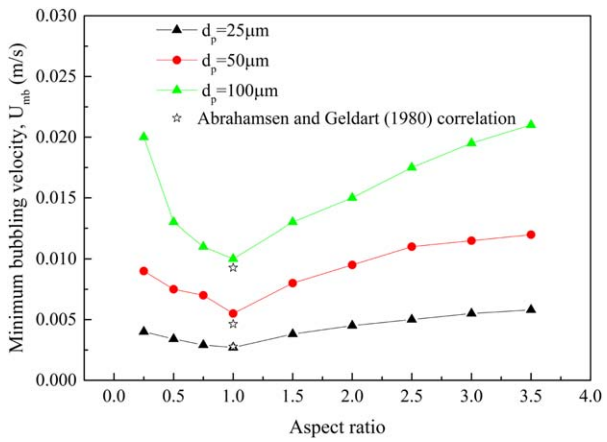


**Figure 15. Effect of particle shape on the minimum bubbling velocities ($U_{mb}$).**

**[Color figure can be viewed in the online issue, which is available at wileyonlinelibrary.com.]**

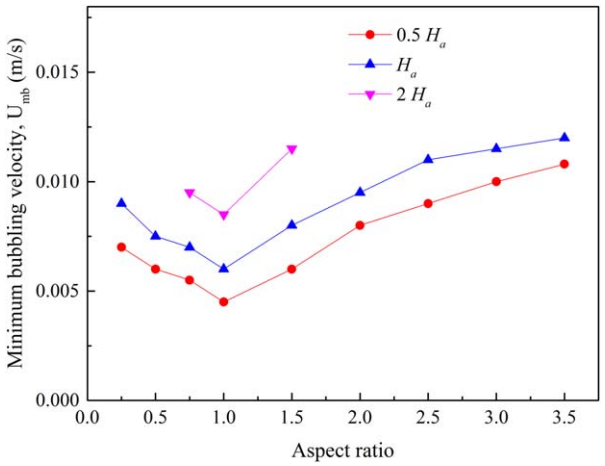


**Figure 16. Effect of Hamaker constant ($H_a$) on minimum bubbling velocity ($U_{mb}$) for different aspect ratios ($H_a = 2.1 \times 10^{-21}$ J).**

**[Color figure can be viewed in the online issue, which is available at wileyonlinelibrary.com.]**

ratio, $\alpha$, is used to represent the particle shape factor rather than sphericity, $\phi$. The new correlation is given below

$$U_{mf} = \frac{(\rho_p - \rho_g) g \varepsilon_{mf}^{3.041} \alpha^{0.298} d_p^{2.06}}{78.89(1-\varepsilon_{mf})\mu_g} \tag{11}$$

As shown in Figure 13, the equation fits the simulation data well. From the exponents of the correlation, it can be seen that the effect of particle size on $U_{mf}$ overweighs that of particle shape.

Agbim et al.[71] found that the presence of interparticle forces suppresses bubbling in gas-fluidized bed. Pandit et al.[72] reported that $U_{mf}$ is independent of interparticle forces while $U_{mb}$ is increasing with increasing cohesive force. The bed expansion is found to increase with increasing interparticle cohesive force, but the expansion rate is independent of interparticle forces. The effect of Hamaker constant $H_a$ on minimum fluidization velocity $U_{mf}$ is examined in this work for fine ellipsoids, and the results are shown in Figure 14. For nearly spherical particles with aspect ratio between 0.75 and 1.5, with the increase of Hamaker constant, there is almost no change in $U_{mf}$, which is consistent with the findings of Pandit et al.[72] For very flat or elongate particles, however, $U_{mf}$ increases significantly with $H_a$.

*Minimum Bubbling Velocity.* For Geldart A particles, there is an interval of homogeneous expansion before the onset of bubbling fluidization. The gas velocity where the heterogeneously bubbling structure appears is defined as the minimum bubbling velocity ($U_{mb}$), demarcating the homogeneous and heterogeneous fluidization regimes. For large coarse particles, no bubbles occur before the bed fluidized, and $U_{mb}$ equals $U_{mf}$.

In physical experiments, there are several ways to determine $U_{mb}$, as discussed by Hou et al.[20] The first method is based on the direct observation that $U_{mb}$ is the velocity at which the first bubble erupts at the free surface of the bed.[7,16] The second method is based on the expansion characteristics of fluidized beds. $U_{mb}$ is estimated as the gas velocity at which the bed height (or bed voidage) reaches a local maximum.[17,18] The third method is through the change of the spatial fluctuation of expansion behavior, such as local porosity[11] or pressure drop[11,68] of the bed over a range of gas velocities spanning from the fixed bed state to the freely bubbling regime. Wang et al.[11] compared the different methods, and found that $U_{mb}$ from method 3 is the highest, followed by method 1 and then method 2. They concluded that the minimum bubbling velocity is overestimated using method 3 due to the gradual formation and growth of heterogeneous structures, where more and more gas is preferentially passing the bed in the form of bubbles, and less gas passes through the emulsion phase, which causes the contraction of emulsion phase and consequently the occurrence of the bed contraction phenomenon. However, visual observation is always subjective because it depends on how to exactly define a "clearly recognizable bubble." Therefore, in this work, the minimum bubbling velocity is determined when the $\Delta P$-time curve starts to fluctuate. The predicted results are then compared with the well-known experimental correlation by Abrahamsen and Geldart.[7]

Figure 15 shows the effect of particle shape on the minimum bubbling velocities of group A particles. It can be found that although nonspherical particles have a lower $U_{mf}$, a higher $U_{mb}$ is predicted compared with spherical particles for different particle sizes. This is possibly caused by the steric hindrance. That is, a higher gas velocity is required for ellipsoidal particles to trigger fluidization because it needs not only to break the interlocks, but also to make large space to rotate to their preferred orientation.[73] The predicted results of spherical particles agree well with the correlation of Abrahamsen and Geldart.[7]

Figure 16 shows the effect of Hamaker constant $H_a$ on minimum bubbling velocity $U_{mb}$. It can be seen that for different aspect ratios, $U_{mb}$ increases markedly with $H_a$. It should be noted that for the case of 2 $H_a$, some points are missing on the curve. This is because at a gas velocity between 0.01 and 0.015 m/s, the beds are very difficult to fluidize, and expanded bed can only form for nearly spherical particles. Moreover, compared with Figure 14, the influence of $H_a$ on $U_{mb}$ is more obvious than on $U_{mf}$. The range of bed expansion is increasing with cohesive force, especially for nearly spherical particles. This is consistent with the findings of Pandit et al.[72]

The ratio of minimum bubbling velocity to minimum fluidization velocity, $U_{mb}/U_{mf}$, is another fluidization index, which gives a measure of the degree to which the bed can be expanded uniformly.[16] This ratio tends to be relatively high for Geldart Group-A powders.[74] The higher the ratio, the more gas a catalyst can hold between its minimum fluidization and bubbling points.[75]

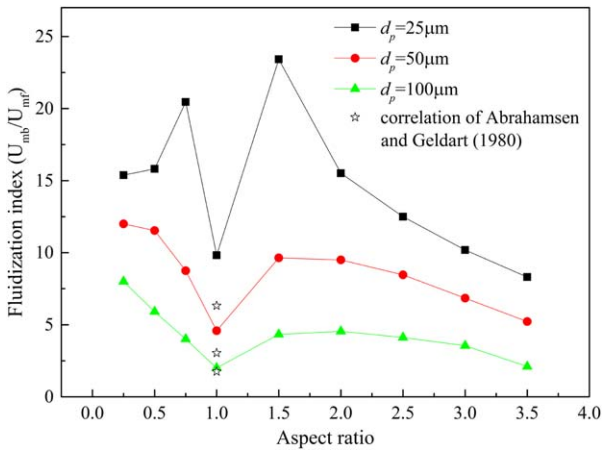


**Figure 17. Effect of particle shape on the fluidization index ($U_{mb}/U_{mf}$).**

**[Color figure can be viewed in the online issue, which is available at wileyonlinelibrary.com.]**

This index can vary from a ratio barely distinguishable from unity to as great as two or so in special cases. With materials such as fine cracking catalyst, the ratio is typically around 1.2.[16]

Figure 17 shows the effect of particle shape on the fluidization index ($U_{mb}/U_{mf}$) of group A particles. Much lower fluidization index is obtained for spherical particles. These results are quite close to the simulated results of Hou et al.,[20] but higher than the predicted by the correlation of Singh and Roy.[16] Specifically, for oblate particles of 50 and 100 $\mu$m, the fluidization index increases significantly when aspect ratio reduces. This indicates that oblate particles need a larger velocity range in the expanded bed regime, and more bubbles can be held in the disc-like particle systems. Oblate particles tend to pile up to form enclosed voids. Therefore, to reach the fluidized bed regime, the bed must first expand to make enough room for bubbles to break the initial pileup state and trigger fluidization. For even a smaller particle size ($d_p = 25$ $\mu$m), the minimum bubbling velocities are quite close to each other for different aspect ratios as shown in Figure 13, so the fluidization index is mainly determined by minimum fluidization velocity. Therefore, the fluidization index-aspect ratio curve shows a "M" shape, corresponding to the "W" shape in Figure 13d. To be specific, the aspect ratio for highest fluidization index is 0.5 for oblate and 1.5 for prolate particles. When aspect ratio further increases from 1.5, the fluidization indices decrease quickly. This indicates that bubbles are difficult to be held in the bed. After reaching the expanded bed regime, a small increase in gas velocity will lead to the fluidized bed regime. Furthermore, smaller particles have higher fluidization index, indicating that smaller cohesive particles have worse flowability.

## Conclusions

CFD–DEM approach has been extended in this work to study the macro-scale flow behavior of fine ellipsoids in gas fluidization. In addition to the normal contact forces, the van der Waals force model is obtained from an interaction potential for ellipsoids to take into account the combined effect of particle size, shape, and orientation on fluidization. The following conclusions can be drawn from this study:

- Agglomerates with different shapes can be observed in gas fluidization of fine ellipsoids. The agglomerate size increases with the decrease of particle size. For fine prolate spheroids, "chain phenomenon," as a special shape of agglomerates, exists in both expanded and fluidized beds. The necessary conditions for "chains" to form are: large enough van der Waals force, elongated particle shape, particles velocities largely in the same directions, and enough void space.
- In expanded bed, there is an obvious pressure drop fluctuation before pressure drop levels off at bed weight per unit area, as a result of the separation of the bulk into two parts and descending impact of the upper part. The more the particles are nonspherical, the higher the fluctuation amplitude. The fluctuation amplitude of pressure drop in fluidized bed of ellipsoids grows with particle size, but slightly varies with particle shape.
- The minimum fluidization velocity increases exponentially with the increase of the particle size. The minimum fluidization velocity vs. aspect ratio curves show largely a "W" shape; with particle size decreasing, the wings of the "W" become upturned, especially for the prolate particles, implying the poor flowability of prolate spheroids. A modified correlation on minimum fluidization velocity is obtained based on the Ergun equation[65] by considering the effects of both particle size and shape. Consistent with Pandit et al.,[72] for nearly spherical particles, minimum fluidization velocity is independent of van der Waals force. But for very flat or elongated particles, minimum fluidization velocity increases with Hamaker constant.
- A higher minimum bubbling velocity is predicted for ellipsoidal particles, compared with spherical particles, because it needs not only to break the interlocks among particles, but also to make large space to rotate to their preferred orientation. Minimum bubbling velocity increases significantly with Hamaker constant. Fluidization index increases with the decrease of particles size. More bubbles can be held for disc-like particles, but difficult for elongated particles.

## Acknowledgments

The authors are grateful to the Australian Research Council for the financial support of this work, and the NCI National Facility for the support in computation.

## Literature Cited

1. Donsì G, Massimilla L. Bubble-free expansion of gas-fluidized beds of fine particles. *AIChE J*. 1973;19(6):1104–1110.
2. Wang Z, Kwauk M, Li H. Fluidization of fine particles. *Chem Eng Sci*. 1998;53(3):377–395.
3. Ye M, van der Hoef MA, Kuipers JAM. The effects of particle and gas properties on the fluidization of Geldart A particles. *Chem Eng Sci*. 2005;60(16):4567–4580.
4. Xu C, Zhu J. Parametric study of fine particle fluidization under mechanical vibration. *Powder Technol*. 2006;161(2):135–144.
5. Galvin JE, Benyahia S. The effect of cohesive forces on the fluidization of aeratable powders. *AIChE J*. 2014;60(2):473–484.
6. Geldart D. Types of gas fluidization. *Powder Technol*. 1973;7(5):285–292.
7. Abrahamsen AR, Geldart D. Behaviour of gas-fluidized beds of fine powders part I. Homogeneous expansion. *Powder Technol*. 1980;26(1):35–46.
8. Rowe PN, Foscolo PU, Hoffmann AC, Yates JG. Fine powders fluidised at low velocity at pressures up to 20 bar with gases of different viscosity. *Chem Eng Sci*. 1982;37(7):1115–1117.
9. Castellanos A, Valverde JM, Pérez AT, Ramos A, Watson PK. Flow regimes in fine cohesive powders. *Phys Rev Lett*. 1999;82(6):1156–1159.
10. Bahramian A, Olazar M. Fluidization of micronic particles in a conical fluidized bed: experimental and numerical study of static bed height effect. *AIChE J*. 2012;58(3):730–744.
11. Wang J, van der Hoef MA, Kuipers JAM. CFD study of the minimum bubbling velocity of Geldart A particles in gas-fluidized beds. *Chem Eng Sci*. 2010;65(12):3772–3785.
12. Xu BH, Yu AB. *A new stability criterion for bed expansion of gas fluidisation*. In: *Presented at the 4th World Congress on Particle Technology*, Sydney, Australia, 2002:189.
13. Rhodes MJ, Wang XS, Nguyen M, Stewart P, Liffman K. Onset of cohesive behaviour in gas fluidized beds: a numerical study using DEM simulation. *Chem Eng Sci*. 2001;56(14):4433–4438.
14. Kawaguchi T, Tanaka T, Tsuji Y. Numerical simulation of two-dimensional fluidized beds using the discrete element method (comparison between the two- and three-dimensional models). *Powder Technol*. 1998;96(2):129–138.
15. Mikami T, Kamiya H, Horio M. Numerical simulation of cohesive powder behavior in a fluidized bed. *Chem Eng Sci*. 1998;53(10):1927–1940.
16. Singh RK, Roy GK. Prediction of minimum bubbling velocity, fluidization index and range of particulate fluidization for gas–solid fluidization in cylindrical and non-cylindrical beds. *Powder Technol*. 2005;159(3):168–172.
17. ŚciAĄżko M, Bandrowski J. Effect of pressure on the minimum bubbling velocity of polydisperse materials. *Chem Eng Sci*. 1985;40(10):1861–1869.
18. Jacob KV, Weimer AW. High-pressure particulate expansion and minimum bubbling of fine carbon powders. *AIChE J*. 1987;33(10):1698–1706.
19. Suksankraisorn K, Patumsawad S, Fungtammasan B. Prediction of the minimum fluidization velocity from correlations: an observation. *Asian J Energy Environ*. 2001;2(2):145–154.

20. Hou QF, Zhou ZY, Yu AB. Micromechanical modeling and analysis of different flow regimes in gas fluidization. *Chem Eng Sci*. 2012;84:449–468.
21. Liu B, Zhang X, Wang L, Hong H. Fluidization of non-spherical particles: sphericity, zingg factor and other fluidization parameters. *Particuology*. 2008;6(2):125–129.
22. Zhou ZY, Pinson D, Zou RP, Yu AB. Discrete particle simulation of gas fluidization of ellipsoidal particles. *Chem Eng Sci*. 2011;66(23):6128–6145.
23. Yang J, Wang Q, Zeng M, Nakayama A. Computational study of forced convective heat transfer in structured packed beds with spherical or ellipsoidal particles. *Chem Eng Sci*. 2010;65(2):726–738.
24. Zhu Y. *Particle Shape Effects on Dynamic Load Transfer in Granular Media*. Kensington, USA: Master Thesis University of Rhode Island, 1996.
25. Hilton JE, Cleary PW. The influence of particle shape on flow modes in pneumatic conveying. *Chem Eng Sci*. 2011;66(3):231–240.
26. Hilton JE, Mason LR, Cleary PW. Dynamics of gas–solid fluidised beds with non-spherical particle geometry. *Chem Eng Sci*. 2010;65(5):1584–1596.
27. Escudié R, Epstein N, Grace JR, Bi HT. Effect of particle shape on liquid-fluidized beds of binary (and ternary) solids mixtures: segregation vs. mixing. *Chem Eng Sci*. 2006;61(5):1528–1539.
28. Oschmann T, Vollmari K, Kruggel-Emden H, Wirtz S. Numerical investigation of the mixing of non-spherical particles in fluidized beds and during pneumatic conveying. *Procedia Eng*. 2015;102:976–985.
29. Haider A, Levenspiel O. Drag coefficient and terminal velocity of spherical and nonspherical particles. *Powder Technol*. 1989;58(1):63–70.
30. Ganser GH. A rational approach to drag prediction of spherical and nonspherical particles. *Powder Technol*. 1993;77(2):143–152.
31. Hölzer A, Sommerfeld M. New simple correlation formula for the drag coefficient of non-spherical particles. *Powder Technol*. 2008;184(3):361–365.
32. Zhu HP, Zhou ZY, Yang RY, Yu AB. Discrete particle simulation of particulate systems: theoretical developments. *Chem Eng Sci*. 2007;62(13):3378–3396.
33. Zhu HP, Zhou ZY, Yang RY, Yu AB. Discrete particle simulation of particulate systems: a review of major applications and findings. *Chem Eng Sci*. 2008;63(23):5728–5770.
34. Zhou ZY, Kuang SB, Chu KW, Yu AB. Discrete particle simulation of particle–fluid flow: model formulations and their applicability. *J Fluid Mech*. 2010;661:482–510.
35. Launder BE, Spalding DB. The numerical computation of turbulent flows. *Comput Methods Appl Mech Eng*. 1974;3(2):269–289.
36. Zhou ZY, Yu AB, Zulli P. Particle scale study of heat transfer in packed and bubbling fluidized beds. *AIChE J*. 2009;55(4):868–884.
37. Kuang SB, Yu AB. Micromechanic modeling and analysis of the flow regimes in horizontal pneumatic conveying. *AIChE J*. 2011;57(10):2708–2725.
38. Bellani G, Variano EA. Slip velocity of large neutrally buoyant particles in turbulent flows. *New J Phys*. 2012;14(12):125009.
39. Zhou ZY, Zou RP, Pinson D, Yu AB. Dynamic simulation of the packing of ellipsoidal particles. *Ind Eng Chem Res*. 2011;50(16):9787–9798.
40. Zheng QJ, Zhou ZY, Yu AB. Contact forces between viscoelastic ellipsoidal particles. *Powder Technol*. 2013;40:25–33.
41. Hamaker HC. The London-van der Waals attraction between spherical particles. *Physica IV*. 1937:1058–1072.
42. Everaers R, Ejtehadi MR. Interaction potentials for soft and hard ellipsoids. *Phys Rev E Stat Nonlin Soft Matter Phys*. 2003;67(4 Pt 1):417101–417108.
43. Babadi M, Ejtehadi MR, Everaers R. Analytical first derivatives of the RE-squared interaction potential. *J Comput Phys*. 2006;219(2):770–779.
44. Ting JM. A robust algorithm for ellipse-based discrete element modelling of granular materials. *Comput Geotech*. 1992;13(3):175–186.
45. Lin X, Ng T-T. Contact detection algorithms for three-dimensional ellipsoids in discrete element modelling. *Int J Numer Anal Methods Geomech*. 1995;19(9):653–659.
46. Yang R, Zou R, Yu A. Computer simulation of the packing of fine particles. *Phys Rev E Stat Phys Plasmas Fluids Relat Interdiscip Topics*. 2000;62(3):3900–3908.
47. Seville JPK, Tuzun U, Clift R. *Processing of Particulate Solids*. London: Blackie Academic and Professional, 1997.
48. Ergun S. Fluid flow through packed columns. *Chem Eng Prog*. 1952;48(2):89–110.
49. Li L, Ma W. Experimental characterization of the effective particle diameter of a particulate bed packed with multi-diameter spheres. *Nucl Eng Des*. 2011;241(5):1736–1745.
50. Singh R, Saini RP, Saini JS. Nusselt number and friction factor correlations for packed bed solar energy storage system having large sized elements of different shapes. *Sol Energy*. 2006;80(7):760–771.
51. Sommerfeld M, Laín S. Transport characteristics of isometric non-spherical particles in turbulent flows. *El Hombre y la Máquina*. 2008(30):108–177.
52. Rothenburg L, Bathurst RJ. Numerical simulation of idealized granular assemblies with plane elliptical particles. *Comput Geotech*. 1991;11(4):315–329.
53. Džiugys A, Peters B. An approach to simulate the motion of spherical and non-spherical fuel particles in combustion chambers. *Gran Matt*. 2001;3(4):231–266.
54. Lin X, Ng TT. A three-dimensional discrete element model using arrays of ellipsoids. *Geotechnique*. 1997;47(2):319–329.
55. Rahman A, Stillinger FH. Molecular dynamics study of liquid water. *J Chem Phys*. 1971;55(7):3336–3359.
56. Evans DJ, Murad S. Singularity free algorithm for molecular dynamics simulation of rigid polyatomics. *Mol Phys*. 1977;34(2):327–331.
57. Goldstein H, Poole CP, Safko JL. *Classical Mechanics*. San Fracisco, USA: Addison-Wesley Publishing Company, 1980.
58. Xu BH, Yu AB. Numerical simulation of the gas-solid flow in a fluidized bed by combining discrete particle method with computational fluid dynamics. *Chem Eng Sci*. 1997;52(16):2785–2809.
59. Feng YQ, Yu AB. Assessment of model formulations in the discrete particle simulation of gas−solid flow. *Ind Eng Chem Res*. 2004;43(26):8378–8390.
60. Yang W, Zhou Z, Pinson D, Yu A. Periodic boundary conditions for discrete element method simulation of particle flow in cylindrical vessels. *Ind Eng Chem Res*. 2014;53(19):8245–8256.
61. Delaney GW, Hilton JE, Cleary PW. Defining random loose packing for nonspherical grains. *Phys Rev E*. 2011;83(5):051305.
62. Williams SR, Philipse AP. Random packings of spheres and spherocylinders simulated by mechanical contraction. *Phys Rev E*. 2003;67(5):051301.
63. Tsukada M, Ito M, Kamiya H, Horio M. Three-Dimension imaging of particle clusters in dilute gas—solid suspension flow. *Can J Chem Eng*. 1997;75(2):466–470.
64. Davidson JF. Circulating fluidised bed hydrodynamics. *Powder Technol*. 2000;113(3):249–260.
65. Tanaka T, Noma K, Ide Y, Tsuji Y. *Particle clusters formed in dispersed gas-solid flows: simulation and experiment*. In: *Presented at the World Congress on Particle Technology 4 (CD-ROM), 2002*, Sydney, Australia, 2002.
66. Horio M, Kuroki H. Three-dimensional flow visualization of dilutely dispersed solids in bubbling and circulating fluidized beds. *Chem Eng Sci*. 1994;49(15):2413–2421.
67. Svoboda K, Čermák J, Hartman M, Drahoš J, Selucký K. Influence of particle size on the pressure fluctuations and slugging in a fluidized bed. *AIChE J*. 1984;30(3):513–517.
68. Rapagna S, Foscolo PU, Gibilaro LG. The influence of temperature on the quality of gas fluidization. *Int J Multiphas Flow*. 1994;20(2):305–313.
69. Baeyens J, Geldart D. Predictive calculations of fow parameters in gas fluidized beds and fluidization behavior of various powders. In: *Proceedings of the International Symposium on Fluidization and its Applcations*. Toulouse, France, 1973:263–273.
70. Nienow AW, Cheesman DJ. The effect of shape on the mixing and segregation of large particles in a gas-fluidised bed of small ones. In: Grace J, Matsen J, editors. *Fluidization*. New York, USA: Springer, 1980:373–380.
71. Agbim JA, Nienow AW, Rowe PN. Inter-particle forces that suppress bubbling in gas fluidised beds. *Chem Eng Sci*. 1971;26(8):1293–1294.
72. Pandit JK, Wang XS, Rhodes M. Influence of interparticle cohesive force on fluidized bed Behaviour by DEM simulation. In: *Third International Conference on CFD in the Minerals and Process Industries*. Melbourne, Australia: CSIRO, 2003.
73. Campbell CS. Elastic granular flows of ellipsoidal particles. *Phys Fluid*. 2011;23(1):013306.
74. Davidson JF, Harrison D. *Fluidization*. London: Academic Press, 1971.
75. Corporation E. *How Catalyst Characteristics Affect Circulation*. Iselin, NJ: Engelhard, 2000.

*Manuscript received Apr. 13, 2015, and revision received Aug. 28, 2015.*